Published in final edited form as:

Cell. 2022 June 09; 185(12): 2148–2163.e27. doi:10.1016/j.cell.2022.04.011.

Zn regulated GTPase metalloprotein activator 1 modulates vertebrate zinc homeostasis

Andy Weiss[1,8], **Caitlin C. Murdoch**[1,8], **Katherine A. Edmonds**[2], **Matthew R. Jordan**[2,3], **Andrew J. Monteith**[1], **Yasiru R. Perera**[4], **Aslin M. Rodríguez Nassif**[4], **Amber M. Petoletti**[1], **William N. Beavers**[1], **Matthew J. Munneke**[1], **Sydney L. Drury**[1], **Evan S. Krystofiak**[5], **Kishore Thalluri**[2], **Hongwei Wu**[2], **Angela R.S. Kruse**[6], **Richard D. DiMarchi**[2], **Richard M. Caprioli**[6], **Jeffrey M. Spraggins**[6,7], **Walter J. Chazin**[4], **David P. Giedroc**[2,3,*], **Eric P. Skaar**[1,9,*]

[1]Department of Pathology, Microbiology, and Immunology, and Vanderbilt Institute for Infection, Immunology, and Inflammation, Vanderbilt University Medical Center, Nashville, TN 37232, USA.

[2]Department of Chemistry, Indiana University, Bloomington, IN 47405, USA.

[3]Department of Molecular and Cellular Biochemistry, Indiana University, Bloomington, IN 47405 USA.

[4]Departments of Biochemistry and Chemistry, and Center for Structural Biology, Vanderbilt University, Nashville, TN 37240, USA

[5]Cell Imaging Shared Resource, Vanderbilt University, Nashville, TN 37232, USA.

[6]Departments of Chemistry and Biochemistry, and Mass Spectrometry Research Center, Vanderbilt University, Nashville, TN 37235, USA

[7]Department of Cell and Developmental Biology, Vanderbilt University, Nashville, TN 37232, USA

[8]Authors contributed equally to this work

[9]Lead contact

Summary

Zinc (Zn) is an essential micronutrient and cofactor for up to 10% of proteins in living organisms. During Zn limitation, specialized enzymes called metallochaperones are predicted to allocate Zn to specific metalloproteins. This function has been putatively assigned to G3E GTPase COG0523 proteins, yet no Zn metallochaperone has been experimentally identified in any organism. Here,

*Corresponding authors - eric.skaar@vumc.org, giedroc@indiana.edu.

Author Contributions

Conceptualization, A.W., C.C.M., K.A.E., M.R.J., D.P.G., E.P.S.; Investigation, A.W., C.C.M., K.A.E., M.R.J., A.J.M., Y.R.P., A.M.R.N., A.M.P., W.N.B., S.L.D., M.J.M., E.S.K., A.R.S.K., H.W.; Formal analysis, A.W., C.C.M., K.A.E., M.R.J. E.S.K.; Resources, K.T., R.D.D; Supervision, R.D.D., J.M.S., R.M.C., W.J.C., D.P.G., E.P.S.; Writing – original draft, A.W., C.C.M., K.A.E., M.R.J., A.J.M., W.J.C., D.P.G., E.P.S.; writing – review & editing, all authors

Declaration of interests

The authors declare no competing interests.

we functionally characterize a family of COG0523 proteins that is conserved across vertebrates. We identify Zn metalloprotease METAP1 as a COG0523 client, leading to the redesignation of this group of COG0523 proteins as Zn regulated GTPase metalloprotein activator (ZNG1) family. Using biochemical, structural, genetic, and pharmacological approaches across evolutionarily divergent models, including zebrafish and mice, we demonstrate a critical role for ZNG1 proteins in regulating cellular Zn homeostasis. Collectively, these data reveal the existence of a family of Zn metallochaperones and assign ZNG1 an important role for intracellular Zn trafficking.

Graphical Abstract

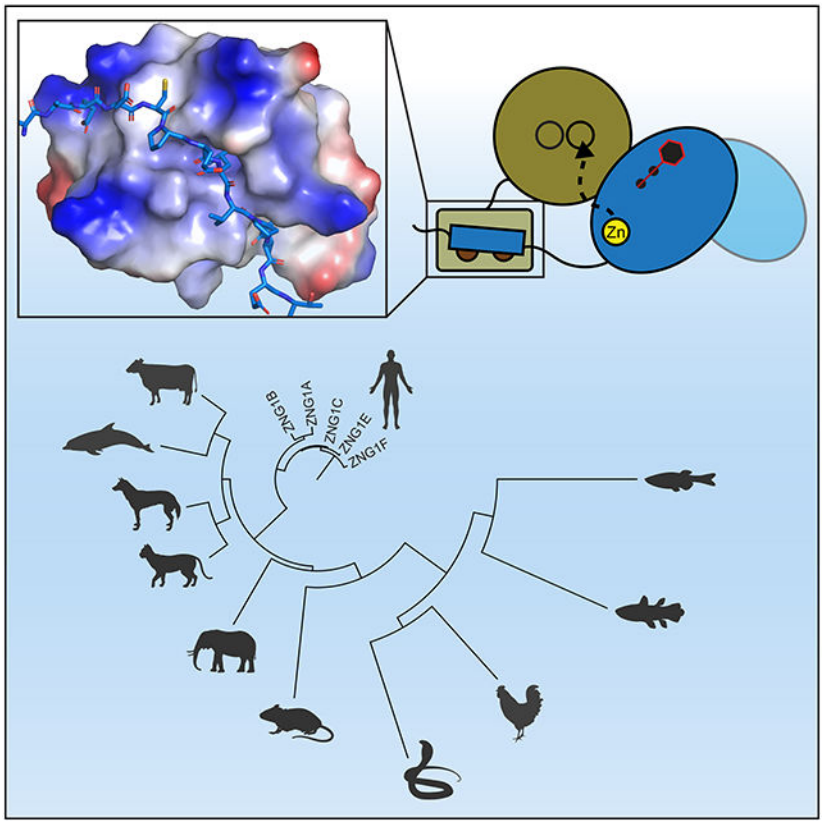

In Brief:

ZNG1 is a putative Zn metallochaperone that supports activity of Zn-dependent proteins in vertebrates, thereby maintaining Zn homeostasis and cellular integrity.

Introduction

Metals are essential micronutrients that are indispensable for cellular processes in all kingdoms of life. Zinc (Zn) is the second most abundant transition metal in humans serving as a structural or enzymatic cofactor for approximately 10% of the proteome (Andreini et al., 2006). Consequently, perturbations in Zn homeostasis are linked to human disease, including growth deficiencies, immune defects, neurological disorders, and cancers (Basu, 2018; Devirgiliis et al., 2007; Fischer Walker and Black, 2004; Prasad, 2013). This is

particularly alarming as Zn deficiency is the fifth most important risk factor for mortality in developing countries affecting close to half of the world's population (Guilbert, 2003).

Cellular Zn is present at levels similar to major metabolites like ATP. However, the majority of Zn within the cell is associated with Zn-requiring metalloproteins, Zn-storage proteins, or maintained in vesicular storage (Krezel and Maret, 2017; Sigel et al., 2013; Wellenreuther et al., 2009), resulting in extremely low levels of freely available Zn (Ba et al., 2009). During Zn limitation, the metalation of critical metalloproteins is thought to require the hierarchical distribution of Zn to ensure their function. Akin to other metals like copper (O'Halloran and Culotta, 2000), targeted transfer of Zn to metalloproteins is hypothesized to be mediated by specialized proteins referred to as metallochaperones (Rosenzweig, 2002), yet no such protein has been identified to date.

Members of the ubiquitous G3E family of P-loop GTPases deliver/insert different metal cofactors to client metalloproteins (Haas et al., 2009). This family includes COG0523 proteins, a poorly understood subgroup found across all branches of life (Edmonds et al., 2021; Haas et al., 2009). COG0523 proteins are characterized by a conserved N-terminal GTPase domain and GTP hydrolysis is thought to provide energy for the transfer of metals to client proteins (Jordan et al., 2019). Furthermore, COG0523 proteins have been linked to cellular Zn homeostasis as the expression of several bacterial and eukaryotic COG0523 members is induced during conditions of Zn starvation (Coneyworth et al., 2012; Haas et al., 2009; Jordan et al., 2019; Mortensen et al., 2014; Ogo et al., 2015). Despite the assignment of COG0523 proteins as putative nucleotide hydrolysis-powered Zn metallochaperones, conclusive experimental evidence in support of this proposed function has not been established.

In this manuscript, we investigate a conserved family of vertebrate COG0523 proteins formerly referred to as CobW-domain containing proteins (CBWDs). Based on the shared function of CBWD in vertebrates and yeast (YNR029c, Pasquini et al.), we have named this protein family ZNG1 for Zn regulated GTPase metalloprotein activator 1. Yeast-two-hybrid screens using homologs in zebrafish (Zng1), mouse (ZNG1), and human (ZNG1E) identified methionine aminopeptidase (METAP1) as a shared ZNG1 client across vertebrates. METAPs perform N-terminal methionine excision (NME), a process that co-translationally removes N-terminal initiator methionine (iMet) for approximately half of newly synthesized peptides contributing to protein stability, maturation, modification, and subcellular localization (Arfin and Bradshaw, 1988; Frottin et al., 2006; Gawron et al., 2016; Gibbs et al., 2014; Giglione et al., 2004; Kim et al., 2014; Meinnel and Giglione, 2008; Polevoda and Sherman, 2003; Varshavsky, 2011). METAPs require a metal cofactor for enzymatic activity, a role often attributed to Zn (Leopoldini et al., 2007; Vetro JA, 2004). Our biochemical and functional characterization of the ZNG1-METAP1 interaction and solution structure of the interacting domains establish a model of METAP1 activation by ZNG1 in a Zn- and GTP hydrolysis-dependent manner, consistent with ZNG1 acting as a metallochaperone. Zebrafish and mouse models of *Zng1* deficiency suggest that ZNG1 supports METAP1 activity *in vivo* and mutation of *Zng1* results in increased sensitivity to dietary Zn starvation. *Zng1* mutation leads to diminished cellular proliferation and mitochondrial dysfunction, resulting in impaired respiration. Collectively these data support

assignment of ZNG1 as a Zn metallochaperone and illustrate the importance of ZNG1 proteins for organismal health and development.

Results

ZNG1s are ancient COG0523 proteins with conserved metalloprotein interactions.

To interrogate the conservation of vertebrate ZNG1 proteins, amino acid sequences spanning an evolutionary distance of over 400 million years were compared (Howe et al., 2021; Kumar et al., 2017). While many vertebrates, including mice and zebrafish, encode for a single ZNG1 protein, five intact ZNG1 paralogs are found in humans (ZNG1A-F with *ZNG1DP* being a pseudogene) (Wong et al., 2004). With over 60% sequence conservation across all analyzed ZNG1 proteins (Figure 1A and S1A), the known catalytic motifs and metal-binding residues of the GTPase domain are uniformly present and conserved (Figure 1B) (Edmonds et al., 2021; Haas et al., 2009). Notably, conserved regions outside of the GTPase domain also are present in the N-terminus (Figure 1B).

Despite broad evolutionary conservation, the functions of COG0523 proteins, including ZNG1, remain unknown in part due to a lack of knowledge of interaction partners. To identify potential client proteins, three independent yeast-two-hybrid screens were performed using full-length zebrafish Zng1, mouse ZNG1, and human ZNG1E proteins as bait. ZNG1E was chosen as the representative human protein due to its consistently high expression across different tissue types and high similarity to the consensus sequence of the human ZNG1 proteins (Figure S1B, C) (Uhlen et al., 2015). Of note, species-specific nomenclature for genes and proteins from the representative backgrounds will be maintained throughout the manuscript (e.g. human: *ZNG1E*, ZNG1E; mouse: *Zng1*, ZNG1; zebrafish: *zng1*, Zng1). Each screen identified at least 9 putative ZNG1 interacting partners (Figure 1C, Table S1). While each dataset revealed species-specific interactions, methionine aminopeptidase 1 (METAP1) was identified in all three screens.

In addition to identifying interaction partners, the yeast-two-hybrid approach also discerned predicted Selected Interacting Domains (SID) of target proteins. SIDs were analyzed to identify the presence of specific protein domains that are partially or completely contained within each SID (Table S1). Enrichment analysis using the dcGO platform (Fang and Gough, (2013) revealed a high prevalence of domains with functions in protein and chromatin binding as well as factors with regulatory roles (Figure 1D). Since *ZNG1* expression is associated with conditions of Zn limitation (Ogo et al., 2015), we hypothesized that ZNG1 aids in the mobilization of cellular Zn during limitation and that proteins with known Zn-binding domains would be interaction partners enriched in these data sets. Indeed, 12 Zn metalloproteins were identified across all three screens, including proteins involved in transcription, protein processing, and the cell cycle (Figure 1E). For most of these proteins, the predicted site of interaction with ZNG1 harbors a Zn finger (zf) motif, including C2H2 (**C**ys$_2$**H**is$_2$), C6H2 (**C**ys$_6$**H**is$_2$), or MYND (**my**eloid, **N**ervy, and **D**EAF-1) (Figure 1F), consistent with known roles of zf domains in facilitating protein-protein interactions (Brayer et al., 2008; Fedotova et al., 2017; Gross and McGinnis, 1996). Because METAP1 was the single conserved ZNG1 interaction identified in all yeast-two-hybrid screens, the METAP1-ZNG1 interaction was selected for additional investigation. To further define the region of

METAP1 that interacts with ZNG1, the results from the three screens were compared to predict a minimal ZNG1-interacting region (Figure 1G), revealing an N-terminal segment of 108 residues containing the C6H2 domain.

The METAP1 C6H2 interacts with a conserved motif in ZNG1.

The interaction of full-length recombinant ZNG1 and METAP1 from mouse and zebrafish was confirmed by affinity chromatography (Figures 2A and S2A-C) and by dynamic light scattering (DLS) (Figure 2B). Masses obtained from DLS for murine ZNG1 and METAP1 individually, as well as for the equimolar complex, were consistent with theoretical masses (Figure 2B). Size exclusion chromatography was performed using murine ZNG1 and N-terminally truncated METAP1$_{1\text{-}83}$ containing the complete C6H2 domain (Figure S2D). The observed shift in elution volume of the 1:1 mixture, compared to individual proteins, indicates that the N-terminus of METAP1 is sufficient to mediate the interaction of ZNG1 with METAP1 (Figures 2C and S2D).

Determination of a minimal binding site on ZNG1 for the interaction with METAP1 was informed by the observation that C6H2 domains resemble MYND domains, with four pairs of conserved cysteine and histidine residues and conserved aromatic residues (Figure S2E-G). No structure has been determined for a C6H2 domain, but structures of MYND domains in AML1/ETO, DEAF-1, and BS69 reveal a ββα architecture, two Zn ions coordinated in an interdigitated pattern, and a binding interface for peptides containing a PxLxP motif (Figure S2E,G) (Harter et al., 2016; Kateb et al., 2013; Liu et al., 2007). The METAP1 C6H2 domain also binds two Zn ions, even when truncated to METAP1$_{1\text{-}59}$ or METAP1$_{1\text{-}79}$, as measured by inductively coupled plasma-mass spectrometry (ICP-MS) (Figure S2H). Moreover, a conserved CPELVPI sequence at the N-terminus of ZNG1 homologs matches the PxLxP motif that MYND binds (Figures 1B and 2D).

METAP1 binding of ZNG1 peptides was confirmed by monitoring quenching of W45 fluorescence in murine METAP1$_{1\text{-}59}$ and METAP1$_{1\text{-}79}$, upon addition of chemically synthesized N-terminal ZNG1 peptides from human, mouse, and zebrafish (Figures 2D,E and S2I). These data reveal a 1:1 binding stoichiometry and a K_D ~ 0.1 μM (Figure 2F-G), which is ≥100-fold tighter than the MYND domains with their cognate peptides (Kateb et al., 2013; Liu et al., 2007). Mouse, human, and zebrafish ZNG1 peptides bound with similar affinities to both METAP1$_{1\text{-}59}$ and METAP1$_{1\text{-}79}$ (Figure 2G), indicating that the N-terminal 59 residues are sufficient for binding. Combined, these findings identify the specific regions of interaction between ZNG1 and METAP1.

NMR spectroscopy was used to explore the interaction in more detail. ^{1}H-^{15}N HSQC spectra of ^{15}N-enriched METAP1$_{1\text{-}59}$ show excellent signal dispersion and uniform intensities indicating a stable, well-folded domain (Figure 2H, left). Addition of a half-molar equivalent of ZNG1 peptide produces a second set of peaks of equal intensity (Figure S2J), indicating a complex in the slow chemical exchange regime on the NMR time scale; addition of a full molar equivalent of ZNG1 peptide reveals a saturated complex. (Figure 2H, middle panel). These results confirm tighter binding than previously observed for MYND domains (Kateb et al., 2013; Liu et al., 2007), and motivate a more detailed analysis of the peptide binding interface.

Solution structure of the METAP1 C6H2 : ZNG1 peptide complex.

An NMR chemical shift perturbation assay was used to identify the METAP1 residues most directly involved in peptide binding. Complete backbone chemical shift assignments for both the peptide-free and peptide-bound states of $METAP1_{1-59}$ (Figure S3A) reveal that residues 21-24 are strongly affected by peptide binding, suggesting direct contact (Figure 2I), while residues 1-18 and 27-32 are relatively unaffected and likely distant from the binding site. Further, chemical shift-based secondary structure predictions reveal that the METAP1 domain has a ββαβα architecture in the free and bound forms (Figure S3B, top, middle), similar to but distinct from the ββα architecture of MYND domains (Figure S2E) (Shen and Bax, 2015). The secondary structure is minimally perturbed by peptide binding.

Further NMR studies of the bound form of $METAP1_{1-59}$ were not possible due to peak splitting for many residues, a limitation circumvented by studying a fusion construct inspired by the structure determination of the AML1/ETO MYND bound to the SMRT peptide (Liu et al., 2007). The ZNG1 peptide was expressed at the N-terminus of $METAP1_{1-59}$ (Figure S3C). The ^{15}N-labeled fusion reproduces the spectra of the bound form with additional crosspeaks for the ZNG1 peptide, but without the multiplets observed previously (Figures 2H and S3D). Minimal perturbations to chemical shifts, localized to the N-terminus of METAP1, validate the utility of the fusion construct (Figures S3A right; S3B bottom; S3E). Moreover, backbone dynamics show that the linker region is flexible and that the dynamics of the domain are consistent in the free and fusion forms (Figures 3A, B and S3F,G). The central region of the peptide encompassing the CPELVPI sequence has elevated heteronuclear NOE values indicative of tight binding. An initial, unrefined NMR structure of the $ZNG1_{10-30}$ $METAP1_{1-59}$ fusion relying exclusively on automated NOE assignments with no additional constraints clearly shows the same cross-brace Zn-binding topology as in a MYND domain. Zn1 is coordinated by C9, C14, C36, and C40 and Zn2 by C22, C25, H48 and H52 (Figure 3C).

The refined solution structure, the first of a C6H2 domain, shows a ββαβα, cross-brace fold with a 1,3,2 antiparallel β-sheet, in which strand 2 hydrogen bonds with the peptide (Figure 3D, Table S2), consistent with the pattern of ^{1}H, ^{15}N chemical shift perturbations (Figure S3H). The negatively charged peptide binds a hydrophobic groove surrounded by a positively charged surface of conserved lysine residues (Figures 3E and S2E-F). In the hydrophobic groove, C18’ and P19’ of ZNG1 make hydrophobic contacts with W45 and F41 in METAP1, L21’ inserts into the pocket lined by F35 and F41, and V22’ and I24’ pack against P23 and Y34, respectively. Sidechains of Q21 and Q38 in METAP1 form hydrogen bonds with the ZNG1 peptide backbone. These data reveal the molecular features of the ZNG1-METAP1 interaction, showing that the high affinity comes from a combination of electrostatic and hydrophobic interactions, as well as hydrogen bonds, consistent with the conservation of these residues in METAP1 and ZNG1 (Figure 3F).

ZNG1 supports METAP1 function in a Zn-dependent manner.

Based on our previous work with bacterial COG0523 proteins, we hypothesize that ZNG1 uses GTP hydrolysis to transfer Zn from the high affinity CxCC binding site into the METAP1 active site, thereby restoring METAP1 activity under conditions of low cellular

Zn (Jordan et al., 2019). In addition to the two Zn ions coordinated by the C6H2 domain, METAP1 binds two metal ions in the active site (Addlagatta et al., 2005). Recombinant murine METAP1 can therefore be loaded with Zn to four molar equivalents (termed Zn_4METAP1). Removal of Zn by extended exposure to EDTA disrupts the zf fold (Figure S4A,B); however, gentler treatment with chelators including nitrilotriacetic acid (NTA; K_{Zn}≈10 nM) selectively removes metal from the active site while leaving the zf domain intact, generating Zn_2METAP1 (Figure S4C). Mag-fura-2 (mf2) and quin-2 Zn competition experiments with Zn_2METAP1 show two high affinity (K_{Zn1} ≈ 8 pM, K_{Zn2} ≈ 20 pM) and two low affinity Zn binding sites (Figures 4A and S4D). Murine ZNG1 binds three molar equivalents of Zn (Figure S4E,F), with one high affinity site (K_{Zn1} ≈ 5 pM) likely coordinated by the CxCC motif in the core GTPase domain (Figure 4B) (Jordan et al., 2019) and two low affinity sites. Like other COG0523 proteins of the same phylogenetic grouping (Edmonds et al., 2021), GTP hydrolysis is slow and slightly inhibited when Zn is bound solely at the high-affinity site (ZnZNG1) (Figure 4C,S4G) (Sydor et al., 2013). However, ZnZNG1 GTPase activity is stimulated by Zn_2METAP1, while ApoZNG1 is not (Figure 4C).

To assess the effect of ZNG1 on METAP1 activity *in vitro*, we first determined initial rates of aminopeptidase activity for the various Zn-bound forms of METAP1 by quantifying released methionine (Met) from the heptapeptide MAHAIHY, a known METAP1 target (Xiao et al., 2010) (Figure S4H-K). Active site-bound Zn is required for activity as Zn_2METAP1 exhibits no turnover, while Zn_3METAP1 partially recovers the activity of fully active Zn_4METAP1 (Figure 4D). Incubation of ApoZNG1 and Zn_2METAP1 shows no activation of Zn_2METAP1, while addition of ZnZNG1 recovers only small amounts of activity (Figure 4E). ZnZNG1 shows no activation of fully metalated Zn_4METAP1 (Figure S4L), consistent with a regulatory impact only on undermetalated METAP1. We next assessed the nucleotide dependence of ZnZNG1 activation of Zn_2METAP1 by incubation with GTP, GDP, or nonhydrolyzable GTP analog, GDPNP. In the presence of GTP, ZnZNG1 nearly fully activates METAP1, and GTP hydrolysis is required for this activation as ZnZNG1 in the presence of GDPNP exhibited no activation (Figure 4E). Although GDP shows some ZnZNG1-dependent activation of METAP1 above that of ZnZNG1 alone, it is far less than that of GTP (Figure 4E). This could result from a conformational change in ZNG1 after GTP hydrolysis that may facilitate release of Zn into the METAP1 active site (Jordan et al., 2019). We performed the same activation experiments in the presence of NTA to ensure Zn-dependent activation of Zn_2METAP1 is due to Zn transfer from ZNG1 directly to METAP1, rather than from Zn in solution. The GTP-bound form of ZnZNG1 again exhibits significant activation of Zn_2METAP1 above that of NTA-bound Zn, while GDPNP has no effect (Figure 4F). Similarly, ZnZNG1 in the presence and absence of GDP shows only minor activation of Zn_2METAP1 activity (Figure 4F). Zebrafish Zng1 also stimulates apo-Metap1 activity (Figure S4M). Together, these data establish that ZNG1 activates Zn_2METAP1 in a Zn- and GTP hydrolysis-dependent manner (Figure 4G).

Zng1 promotes *in vivo* Metap function in zebrafish.

To study the *in vivo* role of Zng1, we turned to a zebrafish model which encode a single copy of *zng1* (Figure 1A). Based on the reported Zn-dependent repression of

ZNG1 in human cell lines (Coneyworth et al., 2012; Ogo et al., 2015), we first sought to assess *zng1* expression in a zebrafish. To modulate organismal Zn levels, chemical treatment of zebrafish larvae was performed via immersion in system water containing the Zn chelator N,N,N',N'-Tetrakis(2-pyridylmethyl)ethylenediamine (TPEN) resulting in a significant induction of *zng1* transcript in WT larvae (Figure 5A). To investigate Zng1-Metap1 interaction *in vivo*, we generated *zng1* mutant zebrafish (referred to *as zng1*$^{-/-}$) using CRISPR/Cas9 gene editing (Figures 5A, S5A). *zng1* mutant fish survived to adulthood under Zn-replete conditions yet morphometric analysis revealed *zng1* mutant larvae exhibit moderate developmental delay with reduced height at anterior anal fin (HAA), standard length, and snout to vent length at 6 days post fertilization (dpf) (Figures 5B-D, S5B) (Parichy et al., 2009).

We hypothesized a role of Zng1 in maintaining Metap1 function and Zn homeostasis in zebrafish. Zebrafish encode for a single copy of Metap1 with high sequence similarity to mammalian METAP1, and two paralogs of Metap2 (Metap2a and Metap2b). Previous studies indicate functional redundancy between METAP1 and METAP2 suggesting that zebrafish Metap2 paralogs could compensate for decreased Metap1 activity in *zng1*$^{-/-}$ animals (Frottin et al., 2006; Li and Chang, 1995; Xiao et al., 2010). To investigate the effects of impaired Metap1 function on organismal health, Metap1 activity *in vivo* was modulated using pharmacologic inhibition of Metap enzymes in larval zebrafish. WT and *zng1*$^{-/-}$ larvae were exposed to the established METAP1/2 inhibitor Bengamide B in Zn-deplete or replete conditions and survival was monitored over three days (Emilio Quinoa, 1986; White et al., 2017). *zng1* mutant larvae displayed increased sensitivity to Bengamide B with 100% lethality when treated with 1 μM of inhibitor as compared to WT controls which remained viable (Figures 5E, S5C). We hypothesized that inhibition of Metap activity in *zng1* mutant animals would be exacerbated in conditions of low Zn. Indeed, co-treatment of *zng1* mutant larvae with a sublethal dose of Bengamide B (500 nM) and TPEN resulted in decreased viability as compared to treatment with 500 nM Bengamide B alone (Figures 5E, S5C). Notably, WT animals treated with Bengamide B also displayed significantly reduced HAA (Figure S5D) mirroring the defects observed in *zng1*$^{-/-}$ larvae (Figure 5B), indicating a functional link between Zng1 and Metap1 *in vivo*. Combined, these data suggest Metap activity is impaired in *zng1* mutant larvae, especially in Zn-deplete conditions.

To further evaluate Zng1 modulation of *in vivo* Metap1 activity, *metap1* mutant zebrafish were generated by CRISPR/Cas9 (referred to as *metap1*$^{-/-}$) (Figure S5E,F). As expected, pharmacologic inhibition of total Metap activity in *metap1*$^{-/-}$ larvae resulted in significantly higher morphologic abnormalities as compared to WT controls at 6 dpf (Figure 5F,G). These abnormalities included pericardial edema (PCE), yolk sack edema (YSE), uninflated swim bladder (USB), and craniofacial defects (CD) (Figures 5F, S5G) (Raghunath and Perumal, 2018). Importantly, *zng1* mutant larvae exhibited similar defects when exposed to the maximum tolerable dose of Bengamide B (Figures 5H-J, S5H) consistent with a role for Zng1 in the promotion of Metap1 activity *in vivo*.

Finally, to test if Metap1 can compensate for Metap2-inhibition in WT animals but not in *zng1* deficient animals (Frottin et al., 2006; Xiao et al., 2010), the METAP2 specific inhibitor TNP-470 was applied by immersion and larval survival was assessed (Zhang et

al., 2000). Similar to what was observed following treatment with Bengamide B, *zng1*$^{-/-}$ larvae displayed decreased survival compared to WT animals following TNP-470 exposure which became more pronounced in Zn-deplete conditions (Figures 5K, S5I). Cumulatively, these data suggest that Metap1 activity is perturbed in *zng1* mutant larvae and, consequently, the pharmacologic potency of both Metap inhibitors is enhanced in the absence of Zng1, particularly during Zn deprivation.

Zng1$^{-/-}$ mice are sensitive to dietary Zn starvation and display signs of mitochondrial dysfunction.

To investigate the impact of ZNG1 in a mammalian model, *Zng1* mutant mice (referred to as *Zng1*$^{-/-}$) were generated using CRISPR/Cas9. The resulting deletion spanning the annotated start codon as well as 50 amino acids within exon 1 (including the CPELVPI motif) was confirmed at the transcriptional and protein level (Figure S6A-C). *Zng1*$^{-/-}$ animals were viable and did not display anomalies in gross morphology. Nevertheless, breeding patterns showed non-mendelian inheritance (Figures 6A and S6D, E), suggesting that ZNG1 functions in early development. We next assessed if ZNG1 effects Zn homeostasis during conditions of dietary Zn deprivation by administering a low Zn diet to WT and *Zng1*$^{-/-}$ mice. Mice deficient in *Zng1* displayed decreased weight gain when fed a low Zn diet (Figure 6B) yet no difference in food uptake was observed. Notably, both WT and *Zng1*$^{-/-}$ animals gained weight at similar rates when fed a control diet (Figure S6F). While a low Zn diet was shown to effectively decrease Zn levels in various organ systems, differences in organ Zn levels between WT and mutant animals were not observed (Figure S6G). These data suggest that loss of *Zng1* leads to failure to access existing Zn pools, rather than affecting organ-specific total Zn levels.

Due to the importance of METAP1 for maintaining cellular proteostasis (Hu et al., 2006; Jonckheere et al., 2018), the impact of *Zng1* deficiency on the global proteome in Zn-deplete conditions was evaluated (Figure 6C, D). Kidneys were selected for this analysis because ZNG1 proteins are highly expressed in human renal tissue (Figure S1B) (Uhlen et al., 2015). Sixty-three differentially abundant proteins were identified in the *Zng1* mutant compared to the WT control (±2-fold cutoff, Figure 6C, Table S3). Analysis of predicted localizations of these proteins using the UniProt database (UniProt, 2021) suggested that a large number putatively localize to the mitochondria, particularly those with decreased abundance (Figure 6C, D). Ingenuity Pathway Analysis (IPA) was performed to predict cellular processes affected by loss of *Zng1* and revealed that numerous proteins play roles in canonical mitochondrial pathways (Figure 6D) (Kramer et al., (2014). Notably, IPA also indicated that Zn-starved *Zng1* animals experience mitochondrial dysfunction, further suggesting negative effects on mitochondrial integrity. While most of the mitochondrial proteins were decreased in abundance in mutant animals (Figure 6C, D), some proteins in this group were significantly elevated in *Zng1*$^{-/-}$ mice, including the mitochondrial ATPase inhibitory factor 1 (IF1, ATPIF1, +7.2-fold) (Garcia-Bermudez and Cuezva, 2016). ATPIF1 is a main regulator of ATP synthase, and blocks both ATP synthesis and hydrolysis activities (Chen et al., 2014). Subsequent IPA upstream regulator analysis (URA) (Kramer et al., 2014) identified ATPIF as a main regulatory node (*P*-value of overlap = 2.4E-33) with experimental linkage to a subset of (mitochondrial) proteins identified as being negatively

affected by loss of ZNG1 (Figure S6H). To evaluate if changes in protein abundance were solely a result of altered protein processing, transcriptomic analysis of a subset of the most differentially abundant proteins was performed. These data revealed modest alterations in transcript levels, with some changes reaching statistical significance, indicating effects of *Zng1* deficiency at both the transcript and protein level (Figure S6I). Together, these results suggest that ZNG1 is important for maintaining mitochondrial function and organismal homeostasis during Zn starvation.

ZNG1 promotes cellular proliferation and respiration in Zn-deplete conditions.

Given that *Zng1* mutant mice displayed signs of impaired Zn homeostasis as well as disruption of mitochondrial function, a cell culture model was generated to further characterize the role of ZNG1. Murine proximal tubular epithelial cells (TKPTS) were selected as a model since mitochondrial dysfunction was detected in murine $Zng1^{-/-}$ renal tissue, and TKPTS cell lines express both ZNG1 and METAP1 (Figures 7A, B and S7A-C). *Zng1* mutant cells (Figure S7A) were generated using CRISPR/Cas9 and decreased mRNA expression (Figures 7B and S7D) and protein abundance (Figure S7C) of ZNG1 were confirmed. The expression of *Zng1* in TKPTS cells was dependent on Zn availability (Figure 7A). While $Zng1^{-/-}$ and WT cells grew at similar rates in untreated media, growth in the presence of Zn chelator tris(2-pyridylmethyl)amine (TPA) significantly slowed proliferation of the *Zng1* mutant cells compared to WT as measured by increased retention of CellTrace dye (Figures 7C and S7E, F). Of note, exposure of WT TKPTS cells to the METAP1/2 inhibitor Bengamide B similarly reduced cellular proliferation, thereby phenocopying the growth impairment observed in *Zng1* mutant cells in Zn-deplete conditions (Figure S7G). Because ZNG1 supports proper function of METAP1 *in vitro* (Figure 4), we postulated that *Zng1*-deficient cells would display increased sensitivity to METAP inhibition. Due to the overlapping substrate specificity of METAP1 and METAP2, TKPTS cells were exposed to the METAP2-specific inhibitor TNP-470. This strategy increases cellular reliance on METAP1 thereby permitting the evaluation of ZNG1-dependent METAP1 activity. Indeed, $Zng1^{-/-}$ cells exhibited slowed proliferation relative to WT when exposed to TNP-470 (Figures 7D and S7H, I) and complementation with full-length *Zng1* significantly enhanced proliferation of *Zng1* mutant cells (Figure S7J). Notably, decreased proliferation and increased sensitivity to METAP-inhibition have been reported in METAP1-deficient HAP1 cells (Jonckheere et al., 2018), which is consistent with the possibility that defects observed in $Zng1^{-/-}$ cells may in part be mediated by dysregulated METAP1 activity.

To further assess a potential impairment of METAP1 function in the $Zng1^{-/-}$ background, the abundance and iMet-status of the known METAP-substrate 14-3-3γ were probed though proteomic profiling (Towbin et al., 2003). Analysis of WT and $Zng1^{-/-}$ cells grown in Zn-replete and Zn-limiting (TPA-treated conditions) conditions revealed reduced levels of 14-3-3γ in *Zng1* mutant cells (Figures 7E). We hypothesized that this reduction was a result of impaired METAP1-dependent iMet removal, and accordingly detected a trend towards higher iMet retention at the 14-3-3γ N-terminus in TPA treated $Zng1^{-/-}$ mutant cells as compared to WT (Figure S7K). Taken together, these data are indicative of a reduction of METAP1 activity in $Zng1^{-/-}$ cells. To further test if the proteomic changes in the *Zng1* mutant resemble those of METAP-deficient cells, proteomic analysis was performed on WT

cells treated with Bengamide B and the results compared to the TPA-treated *Zng1* mutant cells (Table S4). IPA was performed and significantly affected pathways in both datasets determined. Subsequent comparison of the two analyses showed remarkable overlap of the pathways affected by loss of *Zng1* and pharmacological inhibition of METAP (Figure S7L). Notably, pathways affected in both datasets included oxidative phosphorylation and TCA cycle (Figure S7L), as well as mitochondrial dysfunction (*P*-value(−1og10) of 3 and 10.5 for $Zng1^{-/-}$ and Bengamide B-treated, respectively). Collectively, these findings demonstrate that mutation of *Zng1* phenocopies a METAP-deficient system, and that mitochondrial processes are affected by loss of ZNG1.

The reduced proliferation of *Zng1* mutant cells (Figure 7C,D), in combination with proteomic signatures of mitochondrial distress in $Zng1^{-/-}$ cell lines and mice (Figures 6C and S7L) are consistent with a restriction in mitochondrial energy production. Since mitochondrial morphology reflects function (Picard et al., 2013), Zn starved WT and *Zng1* mutant cells were imaged using transmission electron microscopy (TEM). *Zng1* mutant cells were morphologically distinct (Figure 7F) and displayed a significant change in mitochondrial cross-sectional area (Figure 7G) in the absence of alterations of mitochondrial roundness, suggesting that mitochondria from $Zng1^{-/-}$ cells are swollen (Figure S7M). Additionally, mitochondria of $Zng1^{-/-}$ cells displayed increased electron density (Figure 7H). Similar alterations in mitochondrial morphology have previously been associated with uncoupling of the mitochondrial membrane potential from ATP synthesis (Hackenbrock et al., 1971; Huet et al., 2018; Weissert et al., 2021). Consistent with this, cellular ATP levels quantified from the lysates of $Zng1^{-/-}$ TKPTS cells were decreased compared to WT (Figure 7I). Together, these data suggest that ZNG1 contributes to maintaining mitochondrial metabolic homeostasis, and that a loss of ZNG1 renders cells less capable of sustaining the energy necessary for growth during conditions of stress.

To assess broad changes in oxidative phosphorylation, mitochondrial membrane potential was quantified using tetramethylrhodamine methyl ester (TMRM) at a quenching concentration where a decrease in fluorescence intensity correlates to an increase in membrane potential (Monteith et al., 2013; Scaduto and Grotyohann, 1999). TMRM fluorescence was decreased in $Zng1^{-/-}$ cells compared to WT cells in conditions of Zn starvation, indicating mitochondria within *Zng1* mutant cells are hyperpolarized (Figure 7J and S7N), consistent with reduced ATP synthase activity. Mitochondrial superoxide ($O_2^{-\bullet}$) production, a byproduct of electron leakage during electron shuttling across the inner mitochondrial membrane (Forman and Kennedy, 1974; Loschen et al., 1974), was quantified using the fluorescent dye, MitoSOX. Mitochondrial $O_2^{-\bullet}$ levels in *Zng1* mutant cells were lower compared to WT cells, and this phenotype is exacerbated upon METAP2 inhibition (Figures 7K and S7O-R). These results suggest that electron shuttling is decreased in *Zng1* mutant cells despite hyperpolarization of the mitochondria.

To further interrogate the implications of loss of *Zng1* on oxidative phosphorylation, the oxygen consumption rate (OCR) of WT and $Zng1^{-/-}$ cells grown in media alone or in the presence of TPA was quantified by extracellular flux analysis. While $Zng1^{-/-}$ cells exhibited a trend towards decreased basal and maximal respiration compared to WT cells, pre-treatment of mutant cells with TPA significantly impaired basal and maximal

respiration, ATP production, and proton leak (Figure 7L, M). Notably, *Zng1*$^{-/-}$ cells showed accumulated ATPIF1 puncta colocalizing with mitochondrial structures (Figure S7S), consistent with proteomic analysis of *Zng1* mutant animals (Figure 6C, D). These results support a model whereby loss of *Zng1* negatively effects METAP1 activity, particularly during Zn starvation. In turn, impaired MEATP1-dependent processing of the proteome likely disrupts mitochondrial homeostasis. Specifically, *Zng1* mutant cells display hyperpolarization of the mitochondrial membrane with decreased oxidative phosphorylation, consistent with ATPIF1-dependent inhibition of ATP synthase. Taken together, these findings demonstrate that ZNG1 activates METAP1 activity and ZNG1 plays a critical role in regulating mitochondrial function and energy metabolism during Zn starvation.

Discussion

Zn is an essential structural and enzymatic cofactor for many proteins in all branches of life. Consequently, vertebrates have developed sophisticated systems for Zn uptake, intracellular distribution into organelles, and efflux to maintain organismal and cellular Zn homeostasis (Eide, 2006). While numerous aspects of Zn transport and trafficking have been well characterized, mechanisms for allocating Zn within the cell and to individual proteins remain largely unexplored. Distribution of this essential nutrient to “high priority” (Eide, 2006) proteins has been attributed to hypothetical Zn metallochaperones. However, functionally validated interactions with target proteins and *bona fide* Zn metallochaperone function have not been reported. In this study, evolutionarily divergent systems were used to establish a role for ZNG1 in regulating cellular Zn homeostasis, identifying METAP1 as a conserved client of ZNG1 and providing mechanistic insights into ZNG1-dependent METAP1 activation. We propose that GTP hydrolysis drives Zn transfer from ZNG1 into the METAP1 catalytic site either through the energy provided by phosphodiester bond cleavage or a conformational change upon hydrolysis, thereby metalating and activating METAP1. The Zn affinities of ZNG1 and METAP1 are similar, suggesting that Zn transfer may have some element of kinetic control; alternatively, GDP modestly lowers the affinity of ZNG1 for Zn, facilitating capture by METAP1. In any case, the Zn- and GTP-dependent activation of METAP1 by ZNG1 is consistent with the assignment of ZNG1 as a metallochaperone.

The ZNG1-METAP1 interactions described in this study are likely to be more broadly conserved across eukaryotes. Consistent with our findings, this interaction was also suggested by a large-scale screen of the human interactome (Huttlin et al., 2015) and identified by a recent study that investigated Zng1p in *Saccharomyces cerevisiae* (Pasquini *et al.*). The ZNG1-METAP1 interaction in vertebrates is mediated by a conserved N-terminal CPELVPI motif in ZNG1 and the C6H2 domain of METAP1. Our solution structure of the interaction domain reveals that the conserved features, including the hydrophobic binding pockets and the electrostatic surface of METAP1 required for ZNG1 binding, may well be shared among other ZNG1 clients or binding partners. Sequence analysis reveals that approximately half of all eukaryotic ZNG1 homologs (Edmonds et al., 2021) share an N-terminal “$[D/E]_n\psi PxLVp$” motif, in which a series of negatively charged residues $[E/D]_n$ are followed by a non-aromatic hydrophobic residue (ψ), and a conserved proline, leucine, and valine (Figure 3F). Our structure is consistent with this revised motif; it likely captures key features that describe an evolutionarily conserved ZNG1-METAP1 interaction. Indeed, the

N-terminus of *S. cerevisiae* Zng1p lacks the exact vertebrate CPELVPI motif, but matches the more general "$[D/E]_n\psi$PxLVp" pattern. Although the sequence identity of the yeast and mouse Map1p/METAP1 N-terminal domains is less than 40% (Figure S2E), modeling of the Zng1p-Map1p interaction predicts a nearly identical fold and similar peptide interface (Figure S3I), where positive charges surround a hydrophobic groove and engage negatively charged ZNG1 peptides in both complexes. These findings suggest that our structure of the ZNG1-METAP1 interaction domain may be representative of how evolutionarily distant ZNG1 homologs interact with their targets.

The structure and revised ZNG1 motif also provide insight into what proteins may compete with ZNG1 to perform its metallochaperone function. While many proteins contain a more general PxLxP sequence, very few match the "$[D/E]_n\psi$PxLVp" pattern identified here. One notable candidate is in the C-terminus of the β-subunit of the nascent polypeptide-associated complex (NAC), which protrudes from the ribosome exit tunnel (Gamerdinger et al., 2019; Lin et al., 2020). This motif likely explains how the C6H2 domain localizes METAP1 to the ribosome in the presence of NAC (Nyathi and Pool, 2015; Vetro and Chang, 2002). The high affinity of ZNG1 for METAP1 may enable it to outcompete NAC under conditions of low cellular Zn.

Our zebrafish and mouse models of *Zng1* deficiency link ZNG1 to mitochondrial function, organismal development, and Zn homeostasis. The connection between METAP1 and mitochondrial integrity is not without precedent. A previous study that used transcriptomic and proteomic approaches to characterize the effects of METAP1 loss in human HAP1 cells found changes to mitochondrial transcript and protein levels as a result of *METAP1* mutation (Jonckheere et al., 2018). Such data offer a potential explanation as to how mutation of *Zng1* in TKPTS cells results in mitochondrial dysfunction and attenuated cellular respiration, and ultimately explain the detrimental effects observed in *Zng1* deficient animals. Collectively, these findings highlight the importance of ZNG1 for survival during Zn limitation, likely by ensuring functional METAP1-dependent NME and maintaining animal energy balance during such conditions.

In conclusion, we established the vertebrate COG0523 ZNG1 protein family as a major feature of the vertebrate adaptive response to severe Zn deprivation. While these data show a clear physical interaction between ZNG1 and the metalloprotein METAP1, we also provide structural insights into how ZNG1 could interact with other targets. These findings reveal an evolutionary conserved strategy to ensure targeted Zn distribution to a network of high-priority client proteins during conditions of severe Zn starvation.

Limitations of the Study

The current study establishes biochemical and biological details of ZNG1 activation of METAP1. Nevertheless, additional evidence of direct metal transfer from ZNG1 to METAP1 is needed; further, tools are not yet available to probe the METAP1 metalation status *in vivo* as a function of bioavailable Zn. Therefore, this study relies heavily on the functional implications of *Zng1* deficiency in different model systems, all of which strongly suggest a Zn-dependent impairment of METAP1-function in *Zng1* mutants. Overall, these

limitations highlight a future demand for more detailed exploration of both the biological and biophysical underpinnings of ZNG1 activity.

The catalytic GTPase domain is conserved in all COG0523 proteins; thus the contribution of ZNG1 GTPase activity to its cellular function must be further characterized. Although METAP1 activates ZNG1 GTPase activity, hydrolysis is surprisingly low *in vitro* and may suggest additional unidentified accessory proteins. Additionally, the exact roles of nucleotide binding/hydrolysis remain to be explored, as well as the atomic details of the interaction between the catalytic domains of ZNG1 and METAP1, and whether the low affinity Zn binding sites in both proteins play any role in Zn transfer. Moreover, due to the likelihood that ZNG1 proteins support a variety of critical Zn-dependent proteins and essential cellular functions, future studies are required to determine the entirety of the ZNG1 interactome while elucidating what we anticipate will be common features of a ZNG1-client protein interaction.

Deconvoluting potential pleiotropic effects resulting from loss of ZNG1 presents an obstacle for the *in vivo* characterization of the ZNG1-METAP1 interaction. Data generated from the yeast-two-hybrid screen in this study suggest that ZNG1 could mobilize Zn to support the function of multiple protein clients in the cell. Consequently, it is possible that the effects observed in our cell culture and animal models upon mutation of *Zng1* are not solely driven by impairment of METAP1. Rather, failure to metalate additional Zn-dependent ZNG1-targets could compound the effects resulting from decreased METAP1 activity after loss of ZNG1. Consequently, while this study describes the downstream effects of *Zng1* mutation (and METAP1 inhibition) on mitochondrial function in detail, the specific mechanisms by which ZNG1 mediates these effects are not yet known.

STAR Methods

RESOURCE AVAILABILITY

Lead Contact—Further information and request for resources and reagents should be directed to and will be fulfilled by the Lead Contact, Eric P. Skaar (eric.skaar@vumc.org).

Materials Availability—All materials generated in this study are available from the Lead Contact upon request.

Data and Code Availability

- Yeast-two-hybrid data are provided within Table S1. Proteomics data are provided within Tables S3 and S4. Additionally, all mass spectrometry proteomics data have been deposited to the ProteomeXchange Consortium via the PRIDE partner repository with the dataset identifier PXD031516. NMR structure information is provided within Table S2 and the structure is deposited on PDB (7SEK). All backbone and side chain chemical shifts have been deposited in the BioMagResBank under accession number 51117 (free), 51118 (bound), and 30956 (fusion) (Ulrich et al., 2008). Backbone relaxation rates have been deposited in the BioMagResBank under accession numbers 51117 (free)

and 51119 (fusion). The AlphaFold2 structural model of the yeast complex is available in ModelArchive at https://modelarchive.org/doi/10.5452/ma-1hnkh.

- Code used in this study is in supplemental methods S1 (Methods S1).
- Any additional information required to reanalyze the data reported in this paper is available from the Lead Contact upon request.

EXPERIMENTAL MODEL AND SUBJECT DETAILS

Ethics Statement—Mouse and zebrafish studies were approved by the Institutional Animal Care and Use Committees of Vanderbilt University Medical Center (protocol numbers M1900043-00 and M1900076-00 respectively) in accordance with the Public Health Service Policy on the Human Care and Use of Laboratory Animals under the Unites States of America National Institutes of Health (NIH) Office of Laboratory Animal Welfare (OLAW).

Zebrafish Husbandry—All zebrafish lines were maintained on a mixed Tübingen (Tü) / AB background on a 14:10 h light:dark cycle in a recirculating aquaculture system. Embryos were collected from natural matings and maintained in embryo medium (0.03% Instant Ocean Sea Salt in RO water) at a density of ≤ 1 larva / mL at 28°C 14:10 h light:dark cycle. At 3 dpf, larvae were split randomly into treatment groups. All larvae used in experiments are of indeterminate sex and between ages 0 – 6 dpf as reported in the figure legends.

Mouse Husbandry and Diet—Experiments were performed using adult age-matched C57BL/6J (Jackson Laboratories) or C57BL/6J *Zng1*$^{-/-}$ (breeding colony) mice. Animals were maintained at the Vanderbilt University Medical Center Animal Facilities and housed in groups of five. For each experiment, *Zng1*$^{-/-}$ mice from multiple litters were included. Mice of both sexes were between 5-13 weeks of age. The exact age as well as the sex of animals used for each individual experiment are denoted in the corresponding figure legends. For routine colony maintenance, mice were fed a standard chow diet (LabDiets; Rodent Chow Diet 5001). For manipulation of organismal Zn levels, mice were fed a defined Zn-free or control diet (Dyets Inc., AIN-93M Purified Rodent Diet with or without Zn supplementation at 29 parts per million). For experimental endpoints, animals were humanely euthanized. All animal experiments were approved and performed in compliance with the Institutional Animal Care and Use Committee (IACUC) of Vanderbilt University.

Cell Culture Conditions—Mycoplasma-negative WT parental TKPTS and pooled *Zng1* CRISPR/Cas9 mutant cells were ordered from Synthego (https://www.synthego.com/). Briefly, cells were propagated in DMEM/F12 50/50 1X (Corning 10-092-CV) supplemented with 7% heat-inactivated fetal bovine serum (R and D Systems, S11150) with insulin (Sigma SLCF5002 – 0.3 mL of 10mg/mL per 500 mL media) under 5% CO_2. Cells were trypsinized and passaged using TrypLE express (Thermo Fisher Scientific, 12605010).

METHOD DETAILS

Yeast-Two-Hybrid Screening and Analysis—All yeast-two-hybrid screens were performed by Hybrigenics Services using full-length human ZNG1E, mouse ZNG1, and

zebrafish Zng1. Murine *Zng1* and human *ZNG1E* sequences were obtained from Genscript (Clone ID OMu12215 and OHu42907 in the pcDNA3.1-C-(k)DYK backbone, respectively). Full length zebrafish *Zng1* was amplified from 6 days post fertilization (dpf) whole larval cDNA with P1 and P2 (Table S5) and cloned into pCRII TOPO (Invitrogen, K465001) and sequence verified by Sanger sequencing. The sequences described above were used as template for the generation of all subsequent *ZNG1* constructs. Yeast-two-hybrid screens to identify interaction partners of ZNG1 proteins from different species were performed on a mixed (A549, H1703, H460) lung tumor cell library (human), an adult kidney library (mouse), or a whole embryo 20 h post fertilization library (zebrafish). Any interacting partners that were scored as experimental artifact were excluded from further analysis.

Recombinant Protein Cloning—Full-length murine *Zng1* was amplified from pcDNA3.1-C-(k)DYK-*Zng1* using primers P3 and P4 (Table S5). PCR products were inserted into the expression vector pLM302 (Center for Structural Biology, Vanderbilt University) containing a 3C protease cleavable N-terminal 6xHis and Maltose Binding Protein (MBP) tag using *Bam*HI and *Eco*RI restriction sites.

Full-length murine *Metap1* was amplified from pcDNA3.1-C-(k)DYK-*Metap1* (Gencript, Clone ID OMu05035) using primer pair P5/P6. Vector pLM302 was linearized by PCR (primers P7/P8, Table S5). Both amplicons were joined using the NEBuilder HiFi DNA Assembly Master Mix (New England Biolabs, E2621S).

A SUMO-tagged, truncated murine $METAP1_{1-83}$ was prepared by amplifying the N-terminal portion of the murine *Metap1* construct using primers P9 and P10 (Table S5). The PCR product was cloned into the expression vector pBG102 carrying a 3C protease cleavable N-terminal 6xHis and SUMO tag (Center for Structural Biology, Vanderbilt University) using the *Bam*HI and *Eco*RI restriction sites.

For peptide, metal-binding, and METAP1 activation studies, murine *Zng1* was amplified using primers P11 and P12 before being cloned into the *Nde*I and *Bam*HI sites in the pHis vector (Sheffield et al., 1999). Mouse *Metap1*, $METAP1_{1-59}$, and $METAP1_{1-79}$ were cloned into the *Nde*I and *Hind*III sites in the pSUMO vector (Peroutka Iii et al., 2011) containing N-terminal 6xHis and SUMO tags using primers P13-P16 (Table S5) via isothermal assembly (Gibson et al., 2009). The fusion of a 21-residue peptide from murine ZNG1 ($ZNG1_{10-30}$) onto the N-terminus of the truncated $METAP1_{1-59}$, used for the NMR structure, was generated by isothermal assembly (Gibson, 2011) of oligonucleotides P17 and P18 (Table S5) into the *Bam*HI site of the $METAP1_{1-59}$ construct.

The full-length zebrafish *zng1* coding sequence was cloned from 6 dpf whole larval cDNA using primers P1 and P2 into pCRII (Invitrogen) as described above (Table S5). Full-length zebrafish *zng1* was subcloned from TOPO pCRII into pLM302 using primer pair P19/P20 (Supplemental Table 2). Full-length zebrafish *metap1* was amplified from 6 dpf whole larval cDNA and cloned into pLM302 using primer pair P21/P22 (Table S5).

All constructs were confirmed by Sanger sequencing. Murine 6xHis-SUMO-tagged $METAP1_{1-83}$ was transformed into *E. coli* C41(DE3). All other constructs were transformed into *E. coli* BL21(DE3) for expression.

Recombinant Protein Expression and Purification—All bacterial expression strains were grown aerobically in Lysogeny Broth (LB) while shaking. Depending on the specific expression vector, media were supplemented with antibiotic to ensure plasmid maintenance, including 50 μg/mL kanamycin, 100 μg/mL ampicillin, or 35 μg/mL chloramphenicol. Bacterial cultures were grown at 37 °C to OD_{600} = 0.6. Protein expression was initiated with the addition of 0.2-1 mM isopropyl β-D-1-thiogalactopyranoside (IPTG), the temperature was lowered to 18 °C, and the cultures allowed to grow for 14-16 h. Cells were harvested by centrifugation at 4,500x g for 15 min at 4 °C and stored at −20 °C prior to protein isolation.

For affinity chromatography, size exclusion chromatography, and dynamic light scattering experiments, the protein was isolated as follows. Bacterial pellets were resuspended in 10 mL lysis/wash buffer (20 mM HEPES (pH 7.5), 150 mM NaCl). Lysozyme (Thermo Fisher Scientific, 89833) was added at a final concentration of 1 mg/mL before incubating on ice for 10 min. Cells were lysed by sonication and cellular debris removed by centrifugation (4 °C, 10,000x g, 30 min). The supernatant was loaded on a pre-washed column containing amylose resin (New England Biolabs, E8021). Columns were washed with 10 volumes of lysis/wash buffer before elution of bound protein with lysis/wash buffer containing 10 mM maltose. Protein purity and quantity was assessed by SDS-PAGE and BCA assay (Pierce, 23225 and 23209). To remove the 6xHis-MBP tag, protein was incubated with HRV 3C protease (Pierce, 88947) for 12-16h (4 °C with agitation). Cleaved tag was removed by loading the mixture on a pre-washed column containing HisPur Cobalt Resin (Thermo Fisher Scientific, 89964). The flow through was collected and protein purity and quantity assessed by SDS-PAGE and BCA assay (Pierce, 23225 and 23209). Purified protein was used immediately or flash frozen and stored at −80 °C.

For peptide-binding, metal-binding, and METAP1 activation assays, ZNG1 and METAP1 were prepared as follows. Cells expressing untagged ZNG1 were resuspended in 25 mM Tris (pH 8.0), 500 mM NaCl, 2.5 mM EDTA, and 5 mM tris(2- carboxyethyl)phosphine (TCEP). Cells were lysed by sonication for 15 min, and the resulting lysate was centrifuged at 13,000x g for 20 min at 4 °C to remove cellular debris. The resulting supernatant was treated with 0.015% polyethylenimine on ice to precipitate nucleic acids, which were removed by centrifugation at 13,000x g for 20 min at 4 °C. The supernatant was treated with 40% ammonium sulfate on ice for 30 min to precipitate ZNG1. The mixture was separated by centrifugation at 13,000x g for 20 min at 4 °C, and the resulting pellet containing ZNG1 was resuspended in 25 mM Tris (pH 8.0), 150 mM NaCl, 2.5 mM EDTA, and 5 mM TCEP. This solution was dialyzed into 25 mM Tris (pH 8.0), 50 mM NaCl, 2.5 mM EDTA, and 5 mM TCEP overnight, injected onto a preequilibrated HiTrap Q FF (Cytiva Life Sciences, 17515601), and eluted with a gradient from 50 mM to 1 M NaCl. Fractions of >90% purity were combined for additional purification by size-exclusion chromatography (HiLoad 16/600 Superdex 200 pg, Cytiva Life Sciences 28989335) in 25 mM Tris (pH 8.0), 150 mM NaCl, 2.5 mM EDTA, and 5 mM TCEP. All fractions of >95% purity (by inspection of SDS PAGE gels) were collected and buffer- exchanged 10^6-fold into chelex-treated (Biorad

141253) 25 mM 4-(2-hydroxyethyl)-1- piperazineethanesulfonic acid (HEPES (pH 7.4)), 150 mM NaCl, and 5 mM TCEP to create the final prep of ZNG1. ZNG1 prepared in this way was devoid of bound metal (<0.01 mol equiv of Zn(II) measured by ICP-MS).

For SUMO-tagged METAP1 constructs, cells were resuspended in 25 mM Tris (pH 8.0), 500 mM NaCl, and 5 mM TCEP. Cells were lysed by sonication for 15 min, and the resulting lysate was centrifuged at 13,000x g for 20 min at 4 °C to remove cellular debris. The resulting supernatant was injected onto a HisTrap FF (Cytiva Life Sciences, 17525501) column and eluted with a gradient from 0 to 500 mM imidazole. Fractions of >90% purity were combined and treated with SUMO protease for 2 h at room temperature to remove the N-terminal His-SUMO tag and dialyzed into 25 mM Tris (pH 8.0), 500 mM NaCl, and 2 mM TCEP. The cleaved protein product was injected onto a HisTrap FF column and the flow through was collected and concentrated for additional purification by size-exclusion chromatography (HiLoad 16/600 Superdex 200 pg for full-length METAP1 or HiLoad 16/600 Superdex 75 pg for truncated METAP1) in 25 mM Tris (pH 8.0), 150 mM NaCl, 2 mM TCEP. All fractions of >95% purity (by inspection of SDS PAGE gels) were collected and full-length protein was treated with chelator as indicated below. Purified protein was buffer-exchanged 10^6-fold into chelexed 25 mM HEPES (pH 7.4), 150 mM NaCl, and 2 mM TCEP to create the final prep of METAP1, $METAP1_{1\text{-}59}$, or $METAP1_{1\text{-}79}$. Notably, we experienced significant decreases in METAP1 enzymatic activity from frozen protein stocks frozen over extended amounts of time (>1 month) and aliquots that had gone through multiple freeze thaw cycles. Therefore, final preparations of full-length METAP1 utilized in *in vitro* experiments in this study were purified, stripped of metal, and aliquoted for −80 °C storage all within one day. Moreover, frozen aliquots were thawed no more than twice to ensure maximal METAP1 enzymatic function. Proteins were analyzed by ICP-MS to identify metal stoichiometries (Figure S2F). To remove excess metal, METAP1 was treated with either 2 mM EDTA, 10 mM NTA, or 4 molar equivalents N,N,N',N-terakis-(2-pyridylmethyl)ethylenediamine (TPEN) for 1 h at 4°C and then buffer-exchanged 10^6-fold into chelexed 25 mM HEPES (pH 7.4), 150 mM NaCl, and 2 mM TCEP. To load Zn(II) into $METAP1_{1\text{-}59}$ and $METAP1_{1\text{-}79}$, 50 μM Zn(II) and 1 mM NTA were added to protein solutions for 1 h at 4 °C and then buffer-exchanged 10^6-fold into chelexed 25 mM HEPES (pH 7.4), 150 mM NaCl, and 2 mM TCEP. Molar extinction coefficients at 280 nm (35410 M^{-1} cm^{-1} for ZNG1, 55350 M^{-1} cm^{-1} for METAP1, 6990 M^{-1} cm^{-1} for $METAP_{1\text{-}59}$, and 17990 M^{-1} cm^{-1} for $METAP1_{1\text{-}79}$) were used to calculate protein concentration.

Uniformly ^{15}N- and $^{15}N^{13}C$-labeled $METAP1^{1\text{-}59}$ and the $ZNG1_{10\text{-}30}$-$METAP1_{1\text{-}59}$ fusion were prepared for NMR experiments using the SUMO tagged constructs as described above, except for the following details: The expression strains were grown in M9 minimal media with 1 g/L ^{15}N ammonium chloride (Cambridge Isotope Laboratories) as the sole nitrogen source and either 4 g/L unlabeled glucose or 2 g/L ^{13}C-glucose (Cambridge Isotope Laboratories) as the sole carbon source. 10 % ^{13}C-labeled protein was prepared using 1 g $^{15}NH_4Cl$, 0.4 g $^{13}C_6$ -glucose, and 3.6 g unlabeled glucose. The lysis buffer was supplemented with EDTA-free protease inhibitor cocktail (Roche). Nickel-loaded HisTrap FF columns were used to isolate the protein from clarified lysate and after cleavage of the SUMO tag. To ensure that the metal binding sites were homogeneously occupied by Zn(II), the protein was exchanged 10^3-fold into Zn-loading buffer (25 mM HEPES, 150 mM NaCl,

pH 7.4, treated with chelex and supplemented with 1 mM nitrilotriacetic acid [NTA], 50 μM Zn(II), and 2 mM TCEP) using an Amicon ultra centrifugal filter unit (3 kDa cut-off), prior to 10^3-fold exchange into NMR buffer (chelex-treated 10 mM sodium phosphate, 150 mM NaCl, pH 7.0, supplemented with 2 mM TCEP). These samples were confirmed by ICP-MS to contain 2.0 equivalents of Zn(II) and less than 0.01 equivalent of Ni(II).

Affinity Chromatography to Determine ZNG1-METAP1 Interaction—To probe the interaction of the full-length proteins, His-tagged-MBP-ZNG1 (Mouse) was isolated as described above. Protein was loaded onto a previously equilibrated Ni-NTA column (Cytiva Lifesciences, 17-5248-05). The column was washed three times with five column volumes of lysis/wash buffer (10 mM Tris (pH 8) 150 mM NaCl). Following the washes, purified METAP1 with the tag cleaved and removed was loaded onto the column and washed three additional times. After washing, the complex was eluted using wash buffer containing 500 mM imidazole. Fractions were visualized on a 4-20% Bis-Tris SDS-PAGE gel. Western Blot (methods described below) using a polyclonal METAP1 antibody (PA5-58202, 1:1,000) was performed to confirm identity of METAP1.

To test the interaction of zebrafish Zng1 and Metap1, His-tagged-MBP-Metap1 was isolated as described above, cleaved with HRV 3C protease (Pierce, 88947) passed through a HisPur Cobalt Resin (Thermo Scientific, 89964) column, and dialyzed in lysis/wash buffer overnight at 4 °C. Subsequently, His-tagged-MBP-Zng1 was purified as described above with the following exception. Following flow through and washing of the amylose resin (New England Biolabs, E8021), purified Metap1 was passed over the column containing immobilized MBP-Zng1 or empty resin as control. Columns were subsequently washed with 100mL of lysis/wash buffer prior to elution and fractions collected. Western blot detection of Zng1 (anti-CBWD1, HPA042813) of wash and elution fractions was performed using methods described below. Densitometry of Zng1 signal in each fraction was measured using Fiji software (Schindelin et al., 2012).

Dynamic Light Scattering—Purified and tag-free murine ZNG1 and METAP1 were incubated for 1 h at 4 °C before the experiments. The individual proteins and the mixture were filtered through 0.1 μm syringe filters to remove dust and trace residual lipid vesicles. Experiments were performed at 25 °C and data were analyzed using Dynamics 7.5 software (Wyatt Technologies). The DLS software calculates an apparent hydrodynamic radius (Rh) via the Stokes-Einstein equation (Stetefeld et al., 2016).

Size Exclusion Chromatography—The interaction of full-length murine ZNG1 with $METAP1_{1\text{-}83}$ was performed by size exclusion chromatography. Recombinant proteins were purified using methods described above and incubated for 1 h at 4 °C followed by passing over a Superdex 200 increase 10/300 GL column (Cytiva Lifesciences, 28990944). The buffer contained 50 mM Tris (pH 8) and 300 mM NaCl and the experiment was performed with a flow rate of 0.5 mL/min. The resulting fractions were separated and visualized by SDS-PAGE.

Immunoblot Detection of ZNG1 and METAP1—For protein isolation, WT and *Zng1* mutant TKPTS cells were washed once with warm PBS, trypsinized as described above,

and transferred into fresh conical tubes. Samples were centrifuged at 200x g for 10 min. Cells were subsequently washed once with PBS and resuspended in 500 µl of cold RIPA buffer (Thermo Fisher Scientific, 89900) supplemented with Halt protease inhibitor (Thermo Fisher Scientific, 78442). Cells were subsequently vortexed for 10 sec and incubated on ice for 20 min prior to centrifugation for 15 min at 15,000x g. Supernatant was transferred into fresh Eppendorf tubes and protein concentration was measured by BCA assay (Thermo Fisher Scientific, 23225). Samples normalized for protein input were separated on SDS PAGE gels in 1X Tris/Glycine/SDS Buffer (Bio-Rad, 1610732) and transferred using a semi-dry method using Bio-Rad trans blot turbo (25V, 1A, 18 min) onto a nitrocellulose membrane (Li-COR, 926-31092). Transfer efficiency was evaluated using staining with Ponceau S solution (Sigma P7170) following manufacturer's protocol. Membranes were washed three times in PBS supplemented with 0.2% tween (PBS-T), rocking for 5 min at room temperature. Blocking was performed using Odyssey (PBS) blocking buffer (Li-COR 927-40000) for 1 h at room temperature and subsequently washed three times with PBS-T. Primary antibodies were applied (anti-CBWD1, Sigma, HPA042813, 1:500 dilution; anti-Tubulin, Cell signaling, 3873S, 1:1,000 dilution; anti-METAP1, Thermo Fisher Scientific PA5-58202, 1:1,000) in Odyssey blocking buffer and incubated overnight at 4 °C rocking. Membranes were washed three times with PBS-T for 5 min at room temperature. Secondary antibody solutions (Li-COR), species specific IR800CW or IR680LT, 1:2,000) were applied in Odyssey (PBS) blocking buffer, and membranes were incubated in the dark for 2 h rocking at room temperature. Following secondary antibody staining, membranes were washed three times with PBS-T and visualized using a ChemiDoc MP Imaging System with appropriate channels for detection.

Murine METAP1 Methionine Aminopeptidase Assay—Methionine aminopeptidase activity was evaluated by quantifying the release of Met from the heptapeptide MAHAIHY (Genscript) as adapted from (Kabir-ud-Din, 2003). Reactions were conducted at 25°C in 25 mM HEPES pH 7.4, 150 mM NaCl, 2 mM TCEP and consisted of 20 nM murine METAP1 with 0, 1, or 2 molar equivalents of Zn. Reactions were initiated with the addition of varying concentrations of MAHAIHY peptide. 50 µL aliquots were taken every 30 sec from 30-150 sec and the reaction was quenched with the addition of 10 µL glacial acetic acid (Supelco, Sigma-Aldrich). 60 µL of 4% w/v ninhydrin (Sigma-Aldrich) in 100% ACN was added to each quenched reaction and incubated at 37 °C for 1 h to detect free Met. The absorbance at 570 nm was measured and the cleaved Met concentration was determined from a standard curve of 10-500 µM Met. All data are reported as the average of triplicate measurements from each evaluated experimental condition. Midpoint and completed reactions were additionally analyzed by LC-ESI-MS to confirm the generation of the expected AHAIHY cleaved peptide product (Figure S4I).

Mag-fura-2 Zn(II) Competition Assays—Experiments were performed using an HP8453 UV–vis spectrophotometer or an ISS PC1 spectrofluorometer at 25.0 °C. Apo-mf2 (Invitrogen) was monitored by measuring the absorbance at 366 nm or by fluorescence emission at 505 nm upon excitation at 366 nm. Zn-mf2 was monitored by measuring the absorbance at 324 nm or the emission at 505 nm upon excitation at 324 nm. Several [protein]/[mf2] values were used for replicate experiments and analyzed globally to better

calculate the stoichiometry. In a typical fluorescence experiment, 1 μM protein and 1 μM mf2 in 2.5 mL were incubated for 10 min in chelexed buffer [25 mM HEPES (pH 7.4), 150 mM NaCl, and 2.5 mM TCEP], and aliquots of Zn(II) were added. The equilibrium time was 2 min between subsequent additions of metal. The peak intensities at 324 and 366 nm from triplicate experiments were globally fit to 1:1, 2:1, 3:1, and 4:1 binding models, with the K_{Zn} value of mf2 fixed to 5 x 10^8 M^{-1} using Dynafit (Kuzmic, 1996). For ZNG1, the 3:1 binding model provided the best fit of the mf2 data alone, whereas the 4:1 binding model provided the best fit of the METAP1 mf2 data. The selected 4:1 binding model was subsequently used for a simultaneous global fit of triplicate mf2 data sets along with triplicate quin2 datasets for METAP1 (Note S1).

Quin-2 Zn(II) Competition Assays—Experiments were performed using an ISS PC1 spectrofluorometer at 25.0 °C by monitoring the fluorescence emission of quin2 at 490 nm upon excitation at 353 nm, with quenching of the 490 nm emission maximum as aliquots of Zn(II) were added. Experiments were performed in triplicate at multiple protein:quin2 ratios. In a typical experiment, 1-2 μM protein and 1-2 μM quin-2 (Sigma 08520) were incubated for 10 min in chelexed buffer [25 mM HEPES (pH 7.4), 150 mM NaCl, and 2.5 mM TCEP] at a total volume of 3 mL, and 0.3 μM aliquots of Zn(II) were added. The equilibrium time was 12 min between subsequent additions of metal. The peak emission intensities at 490 nm from triplicate experiments were globally fit along with triplicate mf2 datasets using Dynafit (Kuzmic, 1996), with the K_{Zn} value of quin2 fixed to 2×10^{11} M^{-1}.

Intrinsic Trp Fluorescence Quenching Assays—Peptide binding experiments were performed using an ISS PC1 spectrofluorometer at 25.0 °C. Intrinsic Trp fluorescence was monitored using λ_{ex} = 292 nm and λ_{em} = 350 nm, with quenching of the 350 nm emission maxima as aliquots of ZNG1 peptide were added. Different [$METAP1_{1\text{-}59/1\text{-}79}$] values were used for replicate experiments to better calculate the binding stoichiometry and analyzed globally. In a typical experiment, 5 μM $METAP1_{1\text{-}59/1\text{-}79}$ in 2.5 mL were incubated for 10 min in chelexed buffer [25 mM HEPES (pH 7.4), 150 mM NaCl, and 2.5 mM TCEP], and aliquots of ZNG1 peptide were added. The equilibrium time was 2 min between subsequent additions of ZNG1 peptide. The peak emission intensities at 350 nm from triplicate experiments were globally fit to a 1:1 binding model using Dynafit (Kuzmic, 1996).

EDTA titrations of $METAP1_{1\text{-}56}$ were performed using in a Synergy Neo2 plate reader to monitor Trp fluorescence using λ_{ex} = 292 nm and λ_{em} = 350 nm for a series of EDTA (Alfa Aesar A107130B) concentrations ranging from 0.3 μM to 5 mM, for incubation times ranging from 10 min to 6 h at 25 °C. Intensities from triplicate experiments were globally fit to a 2:1 Zn:$METAP1_{1\text{-}56}$ binding model using DynaFit to give an upper bound estimate of the affinity (Kuzmic, 1996) with the K_{Zn} value of EDTA fixed to 7.6×10^{12} M^{-1}.

ZNG1 Peptide Synthesis—The peptides were prepared as C-terminal amides and acetylated at the N-terminus by Fmoc solid-phase synthesis on Chem matrix Rink-Amide resin and purified by reverse-phase HPLC. Peptides were dried and resuspended in water. Calculated molar extinction coefficients at 214 nm were used to determine peptide concentration.

NMR

Assignments: NMR samples contained 0.5-2 mM uniformly ^{15}N- and $^{15}N^{13}C$-labeled protein, with 10 % v/v D2O and 0.3 mM 2,2-dimethyl-2-silapentanesulfonic acid (DSS) as an internal reference. An equivalent 2 mM, $^{15}N^{13}C$-labeled 100% D_2O sample was prepared by lyophilization of a 100% H_2O sample, followed by resuspension in D_2O (Cambridge Isotope Laboratories). NMR spectra were recorded at 25 °C on a Bruker Avance Neo 600 MHz spectrometer equipped with a cryogenic probe or on a Varian VNMRS 800 MHz spectrometer with a room temperature 5 mm PFG HCN probe in the METACyt Biomolecular NMR Laboratory at Indiana University, Bloomington. Data were collected using Topspin 4.0.9 (Bruker) or VNMRJ 4.2 (Varian), processed using NMRPipe (Delaglio et al., 1995), and analyzed using CARA (http://cara.nmr.ch/doku.php) and NMRFAM-Sparky (Lee et al., (2013), all on NMRbox (Maciejewski et al., 2017).

Backbone chemical shifts were assigned for each state using the following standard triple-resonance experiments: HNcaCB, CBCAcoNH, and HNCO (Sattler, 1999). Chemical shift assignments were not obtained for the C' of K59 or C22 in the free or bound states because an HNCO does not include resonances for C' in terminal residues or in residues preceding proline. An HNcaCO of the fusion construct provided these chemical shifts as well as those of C18 and V22 in the ZNG1 peptide, which also precede proline residues. With one proline in the C6H2 domain and two proline residues in the peptide, 100% of all possible amide ^{1}H, ^{15}N atoms are assigned in all three states. 97% of all possible C' atoms are assigned in the free and bound forms, and 100% in the fusion. 100% of all possible Ca and Cb atoms are assigned in the free domain and fusion, but 98% of all Ca and Cb atoms in the bound form, without assignments for C22 due to chemical exchange broadening. The backbone assignments of $METAP1_{1\text{-}59}$ in the absence of peptide are consistent with and expand upon those previously published for human $METAP1_{1\text{-}83}$ (Rachineni et al., 2015).

Aliphatic side-chain assignments were obtained using HBHAcoNH, HcccoNH-TOCSY, hCccoNH-TOCSY, HcCH-TOCSY, hCCH-TOCSY experiments (Sattler, 1999), while hbCBcgcdHD, hbCBcgcdceHE, and H^{ar}(CC-TOCSY-CGCBCACO)NH for were used for aromatic side-chains (Lohr et al., 2007; Yamazaki T, 1993). The 3D experiments were collected using non-uniform sampling with Poisson gap scheduling (Hyberts et al., 2010), and reconstructed with istHMS (Hyberts et al., 2012). Sidechain assignments of the peptide-C6H2 fusion construct are essentially complete, with the assignment of the single methionine methyl group confirmed by a 3D ^{13}C-NOESY-HSQC. Stereospecific assignments of methyl groups for all 3 valine residues and all 5 leucine residues in the fusion construct were obtained using a combination of high-resolution $^{1}H^{13}C$-HSQC and constant-time $^{1}H^{13}C$-HSQC of a 10% ^{13}C-labeled sample (Hilty et al., 2003). The chemical shifts and protonation states of the Nd and Ne atoms of the two histidine sidechains were assigned using a $^{1}H^{15}N$-HSQC experiment optimized for $^{2}J_{NH}$ transfer (Pelton et al., 1993), demonstrating that the Nd atoms are protonated and the Ne atoms coordinate Zn^{II}. A small number of non-amide exchangeable protons were observed in 3D ^{15}N-NOESY-HSQC spectra of the fusion construct, and were attributed to the $O^{g}H$ hydroxyl groups of Ser58, Ser65, and Thr68. Chemical shifts were analyzed for indications of secondary structure using TALOSN (Shen and Bax, 2015).

Dynamics: NMR relaxation measurements including ^{15}N spin relaxation rates, R_1 and R_2, and ^{1}H-^{15}N heteronuclear NOE (hNOE) values were recorded in an interleaved manner using standard experiments. The relaxation delays used were 0.02, 0.06, 0.10, 0.20, 0.40, 0.60, 0.80, and 1.2 s for R_1 and 0.017, 0.034, 0.051, 0.068, 0.085, 0.102, 0.119, 0.136, 0.153, 0.170, 0.204, and 0.238 s for R_2. Residue-specific R_1 and R_2 values were obtained from fits of peak intensities vs. relaxation time to a single exponential decay function, while hNOE ratios were ascertained directly from intensities in experiments recorded with (2 s relaxation delay followed by 3 s saturation) and without saturation (relaxation delay of 5 s). Errors in hNOE values were calculated by propagating the error from the signal to noise.

Structure Determination: Initial structure calculations were performed with CYANA using automatically assigned NOESY peak lists with no further restraints, revealing the expected cross-brace zinc chelation topology (Guntert, 2004). Zn coordination geometry was defined and maintained for subsequent calculations using distance restraints (Zn-Sg = 2.3 Å and Zn-Ne2 = 1.95 Å). Hydrogen bond restraints were added where supported by NOEs, chemical shift-based secondary structure predictions, and slow rates of hydrogen-deuterium exchange. The structure has been deposited into the Protein Data Bank with accession ID 7SEK.

GTPase Activity Measurements (Malachite Green Assay)—Reactions were run in 25 mM HEPES pH 7.4, 150 mM KCl, 2 mM $MgCl_2$, 2 mM TCEP. 20 μL reactions of 5 μM ZNG1 in the presence or absence of 5 μM Zn and 5 μM Zn_2METAP1 were initiated with the addition of 500 μM GTP (Sigma 10106399001) and incubated at 37 °C for 90 min. GTPase reactions were quenched and inorganic phosphate was detected with the addition of 120 μL of 1 mM malachite green oxalate (Acros Organics), 10 mM ammonium molybdate (Sigma-Aldrich) in 1 M HCl. This reaction was incubated in the dark at ambient temperature for 10 min and then quenched with the addition of 60 μL 35% citric acid. Mixtures were incubated for 10 min and inorganic phosphate concentration was calculated based on the absorbance at 680 nm relative to a standard curve (5-500 μM phosphate, Fluka Analytical).

GTPase Activity Measurements (Coupled Assay)—GTPase activity was measured following a previously described protocol (Ingerman and Nunnari, 2005). Reactions were run in 25 mM HEPES pH 7.4, 150 mM KCl, 2 mM $MgCl_2$, 2 mM TCEP in a total volume of 100 μL and included 4 μM ZNG1, 500 μM GTP (Sigma 10106399001), 260 μM NADH (Sigma N8129), 2 mM phosphoenolpyruvate (Sigma 860077), and 1 μL pre-mixed Pyruvate Kinase / Lactate Dehydrogenase (Sigma P0294) at 37 °C. Reactions were monitored in real time by a decrease in absorbance at 340 nm in a Synergy Neo2 plate reader.

Murine ZNG1 Activation of METAP1 Assay—Activation assays were performed in 25 mM HEPES pH 7.4, 150 mM KCl, 2 mM MgCl2, 2 mM TCEP. 250 μM NTA was included where indicated. 10 μM Zn_2METAP1 was incubated with 25 μM apo or ZnZNG1 (ZNG1 loaded with 0.9 eq, 22.5 μM, Zn) at 37 °C for 1 h. Reactions were diluted 500-fold in 25 mM HEPES pH 7.4, 150 mM NaCl, 2 mM TCEP to a final concentration of 20 nM METAP1 and methionine aminopeptidase activity was assayed as described above by initiating the enzymatic reaction with addition of 750 μM MAHAIHY. When using GTP, GDP, or GDPNP, the activation reaction contained 500 μM of the indicated nucleotide. A

control activation reaction of Zn-NTA contained 22.5 μM and 250 μM NTA in reaction buffer.

Zebrafish Metap1 Methionine Aminopeptidase Activity—A single endpoint assay was used for these experiments. Reaction buffer (20 mM HEPES (pH 7.5), 150 mM NaCl) was chelex treated overnight at 4 °C. 1 μM solutions of zebrafish Metap1 and Zng1 were made in reaction buffer. To strip Zn from the METAP1 active site, 3 μM of TPEN was incubated with 1μM METAP1 at 4 °C for 1 h. To prepare holo-Zng1 (Zn bound), Zng1 was incubated with 10 μM of $ZnCl_2$ for 1 h at 4 °C. As a control, Metap1 was incubated with reaction buffer alone. Following the 1 h incubation, Zng1 and Metap1 were washed four times with chelex-treated reaction buffer using protein concentration columns (Amicon Ultra, UFC500396). After washes, proteins were mixed and incubated at 37 °C for 30 min. Following incubation, 100 μM of the synthetic peptide MAHAIHY (Genscript) was added to reactions and incubated for 90 min at 37 °C. Reactions were stopped by the addition of a final concentration of 2% trifluoroacetic acid and samples were centrifuged at max speed for 5 min. Clear supernatant was transferred into fresh glass vials for HPLC analysis.

Twenty μL of each sample and standard was analyzed on an Agilent 1260 Infinity II system. Analytes were separated by gradient HPLC on a Supelco Ascentis Express C_{18} column (50 x 2.1 mm, 5 μm) with a Phenomenex SecurityGuard C_{18} cartridge (3.2 x 8 mm) at a flow rate of 0.4 mL/min using 0.1 % trifluoroacetic acid in water and 0.1% trifluoroacetic acid in acetonitrile as the A and B mobile phases, respectively. The gradient was held at 0% B for 2 min, then ramped to 100% B over the next 18 min. The column was washed at 100% B for 5 min, then equilibrated to 0% B for 5 min. MAHAIHY and AHAIHY were detected using absorbance at 280 nm, and retention times were confirmed using each standard. Methionine aminopeptidase relative activity was determined by calculating the percent of MAHAIHY converted to AHAIHY using the AUC values at 280 nm for each peptide.

Zebrafish Mutagenesis—Targeted deletion of the *zng1* and *metap1* genes were performed using CRISPR/Cas9 gene editing targeting the second exon of *zng1* and first exon of *metap1* as described elsewhere (Essner, 2016). Briefly, the guide RNA sequences 5’ GACCCACAGCTCAGATCC 3’, targeting zebrafish *zng1* and 5’ AGGTGGGACACTGGAGCT 3’ targeting *metap1* were designed using CRISPRscan (Moreno-Mateos et al., 2015) and were synthesized using the oligo-based method (Yin et al., 2015) (P23-P25 Table S5). Cas9 mRNA was generated from *Xba*I (New England Biolabs) digested pT3TS-nls-zCas9-nls plasmid (Addgene, 46757), and *in vitro* transcribed using mMESSAGE mMACHINE T3 kit (Thermo Fisher Scientific, AM1348) (Jao et al., 2013). A cocktail consisting of 150 ng/μL of nls-zCas9-nls and 120 ng/μL of gRNA, 0.05% phenol red, 120 mM KCl, and 20 mM HEPES (pH 7.0) was prepared, and approximately 1–2 nL was injected directly into the cell of one cell stage Tübingen zebrafish embryos. Mutagenesis was initially screened using Melt Doctor High Resolution Melting Assay (Thermo Fisher Scientific, 4409535), and identified two independent *zng1* alleles which were confirmed as deletions by Sanger sequencing of TOPO-cloned PCR products. Subsequent screening of the Δ11 (allele designation *vu2*) was performed by PCR (primers P26/P27, Table S5) and products were resolved on 2% agarose Tris-Borate-EDTA

(TBE) gels. Screening of the Δ5 allele (allele designation *vu1*) was performed by PCR amplification using primers P26 and P27 (Table S5), followed by purification and *Dpn*II digest (New England Biolabs). All *zng1* mutant alleles result in the loss of a single *Dpn*II restriction site present in the WT sequence. Sanger sequencing identified a 17 base pair deletion in the *metap1* first exon (allele designation *vu3*) which was genotyped by PCR using P28/P29 (Table S5) and resolved on 2% agarose Tris-Borate-EDTA (TBE) gels.

Zebrafish Pharmacological Manipulations—For all experiments larval zebrafish were bred naturally and collected into embryo media and were maintained at 28 °C on a 14/10 h light/dark cycle for duration of experiments. For survival experiments, zebrafish larvae were split into even densities into 6 or 12 multi-well plates in 5 mL or 1 mL embryo media respectively at 3 dpf. Stock solutions of METAP2 inhibitor TNP-470 (Sigma, T1455) and METAP1/2 inhibitor Bengamide B (Santa cruz, sc-397521A) were prepared in ACS-grade DMSO (Fisher Scientific, D136) and TPEN (Sigma, P4413) was prepared in ethanol and stored at −20 °C. TNP-470, Bengamide B, and/or TPEN were applied into embryo media as well as a DMSO and/or ethanol vehicle controls at 3 dpf. Zebrafish survival was monitored daily until 6 dpf and all moribund or dead animals were removed. For RT-qPCR experiments, larvae were split at 3 dpf into groups of 20-30 larvae in 20 mL of embryo media supplemented either 20 μM of TPEN or ethanol vehicle control. For imaging experiments, 6 dpf zebrafish larvae treated with 500 nM to 1 μM of Bengamide B or vehicle control were imaged by a Leica Thunder M205FCA stereomicroscope with a Leica DFC9000 GT camera.

Mouse Mutagenesis—Generation of *Zng1*$^{-/-}$ mice. *Zng1*$^{-/-}$ mice were produced using CRISPR-Cas9 genome editing in a C57Bl/6J strain (The Jackson Laboratory) through the Vanderbilt Genome Editing Resource (Vanderbilt University). Ribonucleoprotein complexes containing crRNA + tracrRNA (ctRNA) and SpCas9 protein (MilliporeSigma) targeting DNA sequences within *Zng1* exon 1 and a single stranded DNA donor containing an *Eco*RI restriction site were delivered by pronuclear injection into 1-cell C57BL/6J embryos. crRNA sequences were crRNA: 5'TGGAGTCACTGGTGTCCTGC crRNA: 5'CCGGGTACTTAGGTAATTAA* and 180 nucleotide ssODN donor sequence: ctagaagagaggccccagcccctacctcgaagattcgtcctcggccaggaggcccgggtgcctgaggagacacggcagccccc cttaGAATTCggacaccagtgactccagaactaaagagctgccgccagtcgcgtttccgcgacaggattcagtcggcgcggg gctgatgatgtcacc. F0 founder animals were screened for precise *Zng1* deletions by standard PCR and restriction fragment length polymorphism assays. Deletions were confirmed by Sanger sequencing and verified by a second round of Sanger sequencing in the heterozygous N1 generation. N1 generation *Zng1*$^{-/-}$ heterozygous mice containing the desired mutation were backcrossed at least three generations into the C57Bl/6J strain to allow for segregation of potential off-target editing events prior to familial breeding to produce homozygous offspring. Genotyping of mice from the *Zng1* mutant breeding colony was performed by Transnetyx using ear punches of individual animals and primer pair P30/P31 (Table S5).

Cell Line Mutagenesis—Targeted deletion of the first exon of murine *Zng1* was performed using the guide RNA 'ATTCCAGTCACAATTGTCAC'. Clonal selection of mutant cells was performed by dilution plating. Individual clonal populations of cells

were subsequently screened using primers P32 and P33 (Table S5) followed by Sanger sequencing of TOPO-cloned PCR products. Two independent mutant clones were identified and harbored a homozygous Δ2/Δ2 base pair deletion (clone 1) and a Δ7/Δ2 base pair deletion (clone 2).

Transfection of *Zng1* Mutant Cells—To generate linearized DNA for transfection, pcDNA3.1-C-(k)DYK-$Zng1_{murine}$ was digested with *Sca*I. Cells were grown to 80-90% confluency in 6-well TC treated plates and transfected with lipofectamine reagent using manufacturer's protocol (Lipofectamine 3000, Invitrogen L3000-008). Briefly, 2.5 μg of linear DNA was mixed with P3000 reagent and opti-MEM media (Gibco, 11058-021) to prepare the DNA solution. DNA solution and lipofectamine reagent solutions were mixed at a 1:1 ratio and incubated for 15 min at room temperature. DNA-lipid complexes were added to cells dropwise and cells were incubated overnight at 37 °C at 5% CO_2. G418 (RPI G64500-10) was added at a concentration of 300 μg/ml in complete DMEM/F12 50/50 complete cell culture media described above. G418 resistant cells were diluted and clonally expanded to identify clonal populations of transfected cells. Expression of full-length ZNG1 was validated using Western blot against ZNG1.

Mass Spectrometry Proteomics of Murine Tissue and Cell Lines—Kidneys were isolated from 11-13-week old C57BL/6 or C57BL/6 $Zng1^{-/-}$ mice that were fed a low Zn diet for 5 weeks. Animals were humanely euthanized, kidneys isolated, and flash frozen in liquid nitrogen. For protein isolation, frozen organs were gently thawed on ice and transferred through a 70 μM sterile cell strainers (Thermo Fisher Scientific, 22-363-548) into 5 mL of ice-cold PBS supplemented with Halt protease inhibitor (Thermo Fisher Scientific, 78430). Filters were flushed an additional two times with PBS with protease inhibitor. Cells were pelleted (4 °C, 400x g, 10 min) and pellets resuspended in 500 μL of RIPA buffer with Halt protease inhibitor (Thermo Fisher Scientific, 78430). Following rigorous vortexing, incubation on ice (10 min), and a second round of vortexing, cellular debris were pelleted by centrifugation (4 °C, 10,000x g, 10 min) and supernatant transferred into fresh tubes for further analysis.

Protein concentrations were determined using the 660 Protein Assay (Pierce, 22660). Equal amounts of protein (200 μg) were processed for LC-MS/MS using s-traps (Protifi) (HaileMariam et al., 2018; Zougman et al., 2014). Briefly, proteins were reduced with dithiothreitol (DTT), alkylated with iodoacetamide (IAA), acidified using phosphoric acid, and combined with s-trap loading buffer (90% MeOH, 100mM TEAB). Proteins were loaded onto s-traps, washed, and finally digested with Trypsin/Lys-C (1:100, w:w; enzyme:protein) overnight at 37 °C. Peptides were eluted and dried with a vacuum concentrator. Peptides were resuspended in H2O/1% acetonitrile/0.1% formic acid for LC-MS/MS analysis.

Peptides were separated using a 75 μm x 50 cm C18 reversed-phase-HPLC column (Thermo Fisher Scientific, 164570) on an Ultimate 3000 UHPLC (Thermo Fisher Scientific) with a 120 min gradient (2-32% ACN with 0.1% formic acid) and analyzed on a hybrid quadrupole-Orbitrap instrument (Q Exactive Plus, Thermo Fisher Scientific). Full MS

survey scans were acquired at 70,000 resolution. The top 10 most abundant ions were selected for MS/MS analysis.

Raw data files were processed in MaxQuant (v 1.6.14.0, www.maxquant.org) and searched against the current UniProt *Mus musculus* protein sequences database. Search parameters included constant modification of cysteine by carbamidomethylation and the variable modifications, methionine oxidation and protein N-term acetylation. Proteins were identified using the filtering criteria of 1% protein and peptide false discovery rate. Protein intensity values were normalized using the MaxQuant LFQ function (Cox et al., 2014).

Label free quantitation analysis was performed using Perseus (v 1.6.14.0), software developed for the analysis of -omics data (Tyanova et al., 2016). LFQ Intensity values were Log2-transformed, and then filtered to include proteins containing at least 60% valid values (reported LFQ intensities) in at least one experimental group. Finally, the missing values in the filtered dataset were replaced using the imputation function in Perseus with default parameters (Tyanova et al., 2016). Statistical analyses were carried out using the filtered and imputed protein groups file. Statistically significant changes in protein abundance are determined using Welch's t-test *P*-values and z-scores.

Mass Spectrometry Proteomic Quantification of ZNG1 Peptides—Murine brain tissue was homogenized in NP40 buffer (50 mM trizma base, 150 mM sodium chloride, 1 mM EDTA, and 1% nonidet 40) using cycles of sonication. Protein concentration was quantified using a Bicinchoninic Acid assay (Sigma Aldrich, QPBCA). For each sample, 10 μg of protein was suspended in 8 M urea containing 50mM ammonium bicarbonate to a final volume of 90 μL. Proteins were reduced using a final concentration of 20 mM dithiothreitol (DTT, Thermo Scientific A39255) at 37 °C for 45 min, followed by alkylation using 20 mM iodoacetamide (IAA, Thermo Scientific A39271) at room temperature for 15 min. Samples were diluted to reduce the concentration of urea to <1 M using 50 mM ammonium bicarbonate and proteins were digested using 1 μg of LysN (Thermo Scientific 90300) at 50 °C for 2 h. Oasis mixed-mode cation exchange (MCX) solid phase extraction cartridges (Waters Corporation, Milford, MA 186000252) were used to remove lipids and other contaminants from the digested peptides. Peptide samples were dried using a centrifugal evaporator.

Dried digested samples were reconstituted in HPLC-grade water containing 0.1% formic acid by vortexing and centrifuged briefly to remove any particulates. A total of 250 ng of each sample was desalted and concentrated using C18 EvoTips (EvoSep EV2001). Liquid chromatography mass spectrometry was performed using an EvoSepOne (EvoSep) coupled to an Orbitrap Fusion (ThermoFisher Scientific) equipped with a Nanospray Flex Ion source. Chromatography was performed using a 15 cm long column containing ReproSil-Pur C18 1.9 μm beads by Dr Maisch C18 and a fused silica emitter tip (20 μm inner diameter) (EvoSep EV1112, EV1111). Peptides were eluted from the column using an EvoSep 20 samples/day Whisper method. Mass spectrometry was performed on an Orbitrap Fusion (ThermoFisher Scientific) equipped with a Nanospray Flex Ion source. MS1 was performed using Orbitrap detection at a resolution of 60,000 with a standard AGC target. Data independent acquisition was performed using quadropole isolation with nonoverlapping

windows of 16 m/z from precursor masses 400-1008 with HCD fragmentation (33% collision energy) and Orbitrap detection with a resolution of 30,000. The normalized peak areas for ZNG1 peptides were calculated using Skyline (MacLean et al., 2010).

Gene Expression Analysis—For RNA isolation from dissected mouse tissue, mice were humanely euthanized, tissues harvested and immediately flash frozen in liquid nitrogen and stored at −80 °C. Mouse tissues were transferred into Lysing matrix B tubes (MP, 6911100) containing 700 μl of RLT buffer (Qiagen, 74104) with 1% (v/v) B-mercaptoethanol. Samples were homogenized by bead beating 6 times for 40 s at 6 m/s. Tubes were kept on ice for 1 min in between steps. Samples were centrifuged and homogenate was added to a fresh tube containing 600 μl of phenol:chloroform:iAA (Fisher Scientific, BP17521-100) then vortexed for 30 s. Samples were spun at max speed for 15 min and the aqueous phase was transferred to a tube containing 700 μl of 100% ethanol. Subsequent isolation steps were performed using the Qiagen RNeasy Kit following manufacturer's protocol (Qiagen). gDNA was depleted from final RNA samples by treatment with TURBO DNA-free Kit (Invitrogen). For RNA isolation from zebrafish, pools of 20–30 whole larvae were collected into 1 mL of TRIzol (Thermo Fisher Scientific, 15596026) and stored at −80 °C. For TKPTS cell lines, cells were washed with PBS and collected with 500 μL TRIzol from multi-well plates and stored at −80 °C. Zebrafish larvae and cell lines were homogenized by passing samples 10–15 times through a 27-gauge needle. RNA was isolated following the manufacturer's protocol with the following modification: a second wash with 70% ethanol (prepared in DEPC-treated H_2O) was performed. RNA was treated with DNaseI following manufacturer's instructions (New England Biolabs, M0303L). cDNA from RNA isolated by any of the methods described above was synthesized using the iScript kit (Bio-Rad, 1708891). RT-qPCR was performed in duplicate-quadruplicate 25 μL reactions using 2X iQ SYBR Green SuperMix (BioRad, 1708882) run on an BioRad CFX96 Real-Time System instrument using gene-specific primers (zebrafish: P34-P39, mice: P40-P43, cell lines: 44-69, Table S5). Data were analyzed with the ΔΔCt method (Livak and Schmittgen, 2001) or presented as relative expression values.

Immunofluorescence—WT and *Zng1* mutant TKPTS cells were seeded onto sterile coverslips in 6-well tissue culture treated multi-well plates. At 60-80% confluency, cells were washed three times with warm phenol red free DMEM (Thermo Fisher Scientific, 21041025) prior to fixation with 4% paraformaldehyde solution (PFA, Alfa aesar, J61899) for 15 min at 37 °C then washed three times for 5 min with PBS. Cells were subsequently permeabilized by incubation in 0.2% Triton X-100 in PBS for 10 min at room temperature. Following permeabilization, cells were washed three times for 5 min with PBS at room temperature. Cells were blocked using Odyssey (PBS) blocking buffer (LI-COR) for 1 h at room temperature or overnight at 4 °C. Primary antibodies were diluted in Odyssey blocking solution and incubated overnight at 4 °C rocking (anti-OxPhos Complex V inhibitor Clone 5E2, Invitrogen A21355, 1:200). Cells were washed three times with PBS for 5 min. Secondary antibodies (Thermo Fisher Scientific) and Hoechst (Invitrogen, H3570) were added to Odyssey blocking buffer (Hoechst, 1:1,000, Alexa -conjugated secondaries 1:2000) and cells were incubated for 2 h rocking at room temperature. Following secondary staining, cells were washed three times with PBS and mounted onto slides with 20 uL of ProLong

Gold antifade reagent (Invitrogen, 2273617). Slides cured in the dark overnight at room temperature prior to imaging. Slides were imaged on the Zeiss LSM 880 using the 63X oil objective (1.40 Plan-APOCHROMAT OIL, WD=0.19mm).

Determination of Metal Levels by Inductively Coupled Plasma Mass Spectrometry (ICP-MS)—Murine tissue was homogenized in PBS supplemented with 1% IGEPAL using a Bullet Blender (Next Advance) at 4 °C. Mouse tissue homogenate were acid digested in 400 μL of Optima grade nitric acid (Thermo Fisher Scientific, A467-500) and 100μL of Ultratrace hydrogen peroxide (Sigma, 95321) at 65 °C for 48 h. After digestion, the acid content was diluted to below 10 % with 3.5 mL of UltraPure water (Invitrogen, 10977-023). Elemental quantification on acid-digested samples was performed using an Agilent 7700 inductively coupled plasma mass spectrometer (Agilent) attached to a Teledyne CETAC Technologies ASX-560 autosampler (Teledyne CETAC Technologies). The following settings were fixed for the analysis Cell Entrance = −40 V, Cell Exit = −60 V, Plate Bias = −60 V, OctP Bias = −18 V, and collision cell Helium Flow = 4.5 mL/min. Optimal voltages for Extract 2, Omega Bias, Omega Lens, OctP RF, and Deflect were determined empirically before each sample set was analyzed. Element calibration curves were generated using ARISTAR ICP Standard Mix (VWR, BDH82026-108). Samples were introduced by peristaltic pump with 0.5 mm internal diameter tubing through a MicroMist borosilicate glass nebulizer (Agilent). Samples were initially up taken at 0.5 rps for 30 s followed by 30 s at 0.1 rps to stabilize the signal. Samples were analyzed in Spectrum mode at 0.1 rps collecting three points across each peak and performing three replicates of 100 sweeps for each element analyzed. Sampling probe and tubing were rinsed for 20 s at 0.5 rps with 2% nitric acid between every sample. Data were acquired and analyzed using the Agilent Mass Hunter Workstation Software version A.01.02.

Transmission Electron Microscopy—WT and *Zng1* mutant TKPTS cells treated with 3 μM TPA (Sigma, 723134) were fixed in 2.5% glutaraldehyde in 0.1 M cacodylate for 1 h at room temperature followed by 24 h at 4 °C. The cells were sequentially postfixed in 1% tannic acid, followed by 1% OsO4, then enblock stained with 1% uranyl acetate. Samples were dehydrated in a graded ethanol series and gradually infiltrated with a Quetol 651 formulation Spurrs resin using propylene oxide as the transition solvent. The resin was polymerized at 60 °C for 48 h. Thin sections were cut using a Leica UC7 ultramicrotome with a nominal thickness of 70 nm and collected onto 300 mesh copper grids. All samples were post-stained with 2% uranyl acetate and lead citrate.

TEM imaging was performed on a Tecnai T12 operating at 100 keV using an AMT nanosprint CMOS camera. Single images were acquired using the AMT Capture Engine software. Images for quantification were acquired using serialEM to acquire montages of entire gridsquares, using identical lens currents between samples. These montages were reconstructed using the IMOD/etomo software suite. Mitochondria size, shape, and electron density quantification was performed using the FIJI ROI manager to manually segmentation all mitochondrial cross-sections within randomly selected cells until at least 100 mitochondria were measured for each treatment.

Flow Cytometry Measurement of Cell Proliferation and Mitochondrial Superoxide—TKPTS cells were seeding at 2,000 to 4,000 cells per well of 24-or 12-well tissue culture treated multi-well plates and incubated overnight at 37 °C. Cells were staining with CellTRACE violet (Invitrogen, C34557) as described by manufacturer's protocol. Briefly, CellTRACE solution was prepared in PBS at a 1:1,000 dilution, added to the cells, and cells were incubated for 20 min at 37 °C. Cells were then washed two times in cell culture media supplemented with 7% FBS, and replaced with fresh cell culture media supplemented with desired chemical treatments (3 μM TPA, Sigma, 723134; 5 μg/ml TNP470, Sigma, T1455; or 50 nM Bengamide B, Santa cruz, sc-397521A). Stock solutions of drugs were prepared in ACS-grade DMSO (Fisher Scientific, D136). For growth in Zn deplete conditions, TPA was chosen because it exhibits lower cytotoxicity towards cell lines compared to other chelators (e.g. TPEN) (Huang et al., 2013; Lo et al., 2020). After three days of growth, cells were stained with MitoTracker far-red (Invitrogen, M22426; 1:2500 dilution for 20 min at 37 °C) and MitoSOX red (Molecular probes, M36008 : 1,1000 for 20 min at 37 °C) following manufacture's protocols. Cells were washed with PBS, trypsinized, and transferred to Eppendorf tubes prior to fixation in 4% PFA (Alfa aesar, J61899). Cells were fixed for 20 min at room temperature, centrifuged at 200x g for 10 min and washed with PBS prior to resuspension in 300 μl FACS buffer (2% FBS, 0.02% sodium azide in PBS). All flow cytometry data were collected using a BD LSRII flow cytometer with FACSDIVA software and analyzed using FlowJo (FlowJo LLC). Samples were gated forward scatter height (FSC-H) by forward scatter area (FSC-A) and side scatter height (SSC-H) by side scatter area (SSC-A) to remove doublet populations. The singlet population was gated SSC-A by FSC-A to isolate live cells. The resulting cell population was then assessed for assay-specific fluorescent markers and the median fluorescence intensity (MFI) quantified.

Seahorse XF96 Cell Mitochondrial Stress Test—8,000 WT or *Zng1* mutant vehicle treated TKPTS cells or TKPTS cells serially passaged in 3 μM TPA (Sigma, 723134) were seeded in individual wells of seahorse plates in complete DMEM-F12 50/50 media described above. Assay was performed according following manufacturer's instructions. Briefly, cells were resuspended in mitochondria assay media (Seahorse Agilent pH 7.4 media + 1 mM pyruvate + 10 mM glucose + 2 mM glutamine). No TKPTS cells were added to the four wells in the corners of the plate as a background control. For the mitochondrial stress test, the cartridge was sequentially loaded with oligomycin (15μM), FCCP (15 μM), and rotenone/antimycin A (5 μM) (diluted in mitochondria assay media) for injection into the wells. To normalize across wells by cell density, the Seahorse plate was imaged using a BioTek Cytation 5. Oxygen consumption and extracellular acidification rates were collected using a Seahorse XFe96 Analyzer and analyzed using Wave Desktop software (Agilent Technologies).

Measuring Cellular ATP Production—Cellular ATP levels were measured from WT and *Zng1* mutant TKPTS cell lysates following manufacturer's protocols (Sigma, MAK113). Briefly, 20,000 cells/well WT and *Zng1* mutant cells were seeded in clear-bottom black 96-well plates (Costar, 3603) and incubated for 36 h at 37 °C under 5% CO_2. ATP levels were measured using Cell Titer Glo 2.0 (Promega, G9241). To normalize to

cell number, cells were incubated with Hoechst (1:1,000 in PBS) for 15 min at 37 °C in cell culture incubator then washed with PBS prior to the addition of 100 μL of fresh PBS. Hoechst signal was measured in the BioTek Cytation 5 (ex/em 350/461). Subsequently, 100 μL of Cell Titer Glo reagent was applied directly to the wells and incubated in the dark for 15 min at room temperature. Luminescence was measured in the BioTeck Cytation 5 and expressed as relative light units (RLU).

Tetramethylrhodamine Methyl Ester (TMRM) Assay—WT and *Zng1* mutant TKPTS cells untreated or treated with 3 μM TPA (Sigma, 723134) were seeded at a density of 4,000 cells / well in clear-bottom black 96-well plates (Costar, 3603) and incubated overnight at 37 °C under 5% CO_2. Adherent cells were stained with MitoTracker deep red (Invitrogen, M22426) as described above. TMRM (Invitrogen, T668) staining solution was prepared following manufacturer's instructions. Briefly 100 mM TMRM was prepared in phenol red-free cell growth medium and was added to adherent cells at a quenching concentration of 200 nM as described previously (Monteith et al., 2013). Cells were incubated for 1-2 h at 37 °C at 5% CO_2. TMRM and MitoTracker fluorescence was measured using a BioTek Cytation 5 (TMRM-ex/em 548 nm/574 nm and MitoTracker- ex/em 644 nm/665 nm). For each genotype and treatment condition, 4-8 independent wells were analyzed and TMRM signal was normalized to MitoTracker signal.

Computational Tools—Sequence analysis, alignments and cladograms were created using CLC Genomics Workbench (version 20.0.1.) (Qiagen). Visualization of pairwise alignments was generated using Sequence Demarcation Tool (SDTv1.2) (Muhire et al., 2014). Structural multiple sequence alignments were generated using ESPript (Robert and Gouet, 2014). An iterative HMMsearch was used to identify variations in the ZNG1 N-terminal motif (Eddy, 2009). HMMsearch was also used to identify matches to the refined motif in yeast, human, mouse, and zebrafish genomes. Sequence logo motifs were generated using WebLogo 3.7.4 (Crooks et al., 2004). AlphaFold2 modeling of the yeast Map1p-Zng1p interaction was performed using the ColabFold AlphaFold2_advanced jupyter notebook with max_recycles set to 48 (Jumper et al., 2021) (Mirdita et al., 2021). Pathway analysis of proteins with significantly altered abundance (as determined by Welch's *t*-test) was performed using the Ingenuity Pathway Analysis tool (IPA, Qiagen).

QUANTIFICATION AND STATISTICAL ANALYSIS

All experiments were repeated at least two times and statistical analyses were performed with GraphPad Prism v.9 or OriginPro. Data are presented as mean ± SEM unless otherwise noted in figure legend. For comparisons between 2 groups a two tailed student's t-test or Mann-Whitney test was applied. For comparisons between 3 or more groups, a one-way ANOVA with Tukey's multiple comparisons test was used. For experiments with 2 independent variables, a two-way ANOVA was performed with Tukey's or Sidak's multiple comparisons test. Significance was set *as* $P < 0.05$, and denoted as: * $P < 0.05$, ** $P < 0.01$, *** $P < 0.001$, **** $P < 0.0001$. Sample sizes are indicated in the figure legends.

Supplementary Material

Refer to Web version on PubMed Central for supplementary material.

Acknowledgements

This research was supported by the NIH grants R01AI150701 and R01AI101171 (E.P.S., W.J.C., D.P.G.), as well as R35GM118157 (D.P.G.), T32ES007028 (A.W., C.C.M.), F32AI157215 (A.W.), F32GM142246 (C.C.M.), F32HL144081 (A.J.M.), T32GM109825 (M.R.J.), T32GM131994 (M.R.J.), T32DK101003 (A.R.S.K.), R01AI138581 and R01AI145992 (J.M.S, R.M.C.). E.P.S. was supported by the Ernest W. Goodpasture Chair in Pathology, and the National Cancer Institute (NCI) Vanderbilt-Ingram Cancer Center Support Grant (P30CA068485). A.W. (18POST33990262) and W.N.B. (18POST34030426) were supported by the American Heart Association. Generation of *Zng1*$^{-/-}$ mice by the Vanderbilt Genome Editing Resource was supported by the Cancer Center Support Grant (CA68485), the Vanderbilt Diabetes Research and Training Center (DK020593), and the Center for Stem Cell Biology. Confocal microscopy and TEM imaging was performed in collaboration with the Vanderbilt Cell Imaging Shared Resource (supported by NIH grants: CA68485, DK20593, DK58404, DK59637 and EY08126). Flow Cytometry at the VUMC Flow Cytometry Shared Resource was supported by the Vanderbilt Ingram Cancer Center (P30 CA68485) and the Vanderbilt Digestive Disease Research Center (DK058404). The funders had no role in the study design, data collections and analysis, decision to publish, or preparation of the manuscript. We are grateful for Rachel Hart's assistance in TEM image collection, and for technical assistance by Sophia A. Kvaal. The authors thank the University of South Florida CDDI Proteomics Facility for their support. We thank the members of the Skaar lab, as well as Dr. Borden Lacy, Dr. Jim Cassat, and Dr. Maulik Patel for critical review of the manuscript.

References

Addlagatta A, Hu X, Liu JO, and Matthews BW (2005). Structural basis for the functional differences between type I and type II human methionine aminopeptidases. Biochemistry 44, 14741–14749. [PubMed: 16274222]

Andreini C, Banci L, Bertini I, and Rosato A (2006). Counting the zinc-proteins encoded in the human genome. J Proteome Res 5, 196–201. [PubMed: 16396512]

Arfin SM, and Bradshaw RA (1988). Cotranslational processing and protein turnover in eukaryotic cells. Biochemistry 27, 7979–7984. [PubMed: 3069123]

Ba LA, Doering M, Burkholz T, and Jacob C (2009). Metal trafficking: from maintaining the metal homeostasis to future drug design. Metallomics 1, 292–311. [PubMed: 21305127]

Basu AK (2018). DNA Damage, Mutagenesis and Cancer. Int J Mol Sci 19.

Brayer KJ, Kulshreshtha S, and Segal DJ (2008). The protein-binding potential of C2H2 zinc finger domains. Cell Biochem Biophys 51, 9–19. [PubMed: 18286240]

Chen WW, Birsoy K, Mihaylova MM, Snitkin H, Stasinski I, Yucel B, Bayraktar EC, Carette JE, Clish CB, Brummelkamp TR, et al. (2014). Inhibition of ATPIF1 ameliorates severe mitochondrial respiratory chain dysfunction in mammalian cells. Cell Rep 7, 27–34. [PubMed: 24685140]

Coneyworth LJ, Jackson KA, Tyson J, Bosomworth HJ, van der Hagen E, Hann GM, Ogo OA, Swann DC, Mathers JC, Valentine RA, et al. (2012). Identification of the human zinc transcriptional regulatory element (ZTRE): a palindromic protein-binding DNA sequence responsible for zinc-induced transcriptional repression. J Biol Chem 287, 36567–36581. [PubMed: 22902622]

Cox J, Hein MY, Luber CA, Paron I, Nagaraj N, and Mann M (2014). Accurate proteome-wide label-free quantification by delayed normalization and maximal peptide ratio extraction, termed MaxLFQ. Mol Cell Proteomics 13, 2513–2526. [PubMed: 24942700]

Crooks GE, Hon G, Chandonia JM, and Brenner SE (2004). WebLogo: a sequence logo generator. Genome Res 14, 1188–1190. [PubMed: 15173120]

Delaglio F, Grzesiek S, Vuister GW, Zhu G, Pfeifer J, and Bax A (1995). NMRPipe: a multidimensional spectral processing system based on UNIX pipes. J Biomol NMR 6, 277–293. [PubMed: 8520220]

Devirgiliis C, Zalewski PD, Perozzi G, and Murgia C (2007). Zinc fluxes and zinc transporter genes in chronic diseases. Mutat Res 622, 84–93. [PubMed: 17374385]

Eddy SR (2009). A new generation of homology search tools based on probabilistic inference. Genome Inform 23, 205–211. [PubMed: 20180275]

Edmonds KA, Jordan MR, and Giedroc DP (2021). COG0523 proteins: a functionally diverse family of transition metal-regulated G3E P-loop GTP hydrolases from bacteria to man. Metallomics 13.

Eide DJ (2006). Zinc transporters and the cellular trafficking of zinc. Biochim Biophys Acta 1763, 711–722. [PubMed: 16675045]

Emilio Quinoa MA, Crews Phillip, and Bakus Gerald J. (1986). Bengamides, heterocyclic anthelmintics from a Jaspidae marine sponge. The Journal of Organic Chemistry 51 4494–4497.

Essner J (2016). Zebrafish embryo microinjection: Ribonucleoprotein delivery using the Alt-R CRISPR-Cas9 System. Coralville, Integrated DNA Technologies.

Fang H, and Gough J (2013). DcGO: database of domain-centric ontologies on functions, phenotypes, diseases and more. Nucleic Acids Res 41, D536–544. [PubMed: 23161684]

Fedotova AA, Bonchuk AN, Mogila VA, and Georgiev PG (2017). C2H2 Zinc Finger Proteins: The Largest but Poorly Explored Family of Higher Eukaryotic Transcription Factors. Acta Naturae 9, 47–58. [PubMed: 28740726]

Fischer Walker C, and Black RE (2004). Zinc and the risk for infectious disease. Annu Rev Nutr 24, 255–275. [PubMed: 15189121]

Forman HJ, and Kennedy JA (1974). Role of superoxide radical in mitochondrial dehydrogenase reactions. Biochem Biophys Res Commun 60, 1044–1050. [PubMed: 4372996]

Frottin F, Martinez A, Peynot P, Mitra S, Holz RC, Giglione C, and Meinnel T (2006). The proteomics of N-terminal methionine cleavage. Mol Cell Proteomics 5, 2336–2349. [PubMed: 16963780]

Gamerdinger M, Kobayashi K, Wallisch A, Kreft SG, Sailer C, Schlomer R, Sachs N, Jomaa A, Stengel F, Ban N, et al. (2019). Early Scanning of Nascent Polypeptides inside the Ribosomal Tunnel by NAC. Mol Cell 75, 996–1006 e1008. [PubMed: 31377116]

Garcia-Bermudez J, and Cuezva JM (2016). The ATPase Inhibitory Factor 1 (IF1): A master regulator of energy metabolism and of cell survival. Biochim Biophys Acta 1857, 1167–1182. [PubMed: 26876430]

Gawron D, Ndah E, Gevaert K, and Van Damme P (2016). Positional proteomics reveals differences in N-terminal proteoform stability. Mol Syst Biol 12, 858. [PubMed: 26893308]

Gibbs DJ, Bacardit J, Bachmair A, and Holdsworth MJ (2014). The eukaryotic N-end rule pathway: conserved mechanisms and diverse functions. Trends Cell Biol 24, 603–611. [PubMed: 24874449]

Gibson DG (2011). Enzymatic assembly of overlapping DNA fragments. Methods Enzymol 498, 349–361. [PubMed: 21601685]

Gibson DG, Young L, Chuang RY, Venter JC, Hutchison CA 3rd, and Smith HO (2009). Enzymatic assembly of DNA molecules up to several hundred kilobases. Nat Methods 6, 343–345. [PubMed: 19363495]

Giglione C, Boularot A, and Meinnel T (2004). Protein N-terminal methionine excision. Cell Mol Life Sci 61, 1455–1474. [PubMed: 15197470]

Gross CT, and McGinnis W (1996). DEAF-1, a novel protein that binds an essential region in a Deformed response element. EMBO J 15, 1961–1970. [PubMed: 8617243]

Guilbert JJ (2003). The world health report 2002 - reducing risks, promoting healthy life. Educ Health (Abingdon) 16, 230. [PubMed: 14741909]

Guntert P (2004). Automated NMR structure calculation with CYANA. Methods Mol Biol 278, 353–378. [PubMed: 15318003]

Haas CE, Rodionov DA, Kropat J, Malasarn D, Merchant SS, and de Crecy-Lagard V (2009). A subset of the diverse COG0523 family of putative metal chaperones is linked to zinc homeostasis in all kingdoms of life. BMC Genomics 10, 470. [PubMed: 19822009]

Hackenbrock CR, Rehn TG, Weinbach EC, and Lemasters JJ (1971). Oxidative phosphorylation and ultrastructural transformation in mitochondria in the intact ascites tumor cell. J Cell Biol 51, 123–137. [PubMed: 5111873]

HaileMariam M, Eguez RV, Singh H, Bekele S, Ameni G, Pieper R, and Yu Y (2018). S-Trap, an Ultrafast Sample-Preparation Approach for Shotgun Proteomics. J Proteome Res 17, 2917–2924. [PubMed: 30114372]

Harter MR, Liu CD, Shen CL, Gonzalez-Hurtado E, Zhang ZM, Xu M, Martinez E, Peng CW, and Song J (2016). BS69/ZMYND11 C-Terminal Domains Bind and Inhibit EBNA2. PLoS Pathog 12, e1005414. [PubMed: 26845565]

Hilty C, Wider G, Fernandez C, and Wuthrich K (2003). Stereospecific assignments of the isopropyl methyl groups of the membrane protein OmpX in DHPC micelles. J Biomol NMR 27, 377–382. [PubMed: 14512734]

Howe KL, Achuthan P, Allen J, Allen J, Alvarez-Jarreta J, Amode MR, Armean IM, Azov AG, Bennett R, Bhai J, et al. (2021). Ensembl 2021. Nucleic Acids Res 49, D884–D891. [PubMed: 33137190]

Hu X, Addlagatta A, Lu J, Matthews BW, and Liu JO (2006). Elucidation of the function of type 1 human methionine aminopeptidase during cell cycle progression. Proc Natl Acad Sci U S A 103, 18148–18153. [PubMed: 17114291]

Huang Z, Zhang XA, Bosch M, Smith SJ, and Lippard SJ (2013). Tris(2-pyridylmethyl)amine (TPA) as a membrane-permeable chelator for interception of biological mobile zinc. Metallomics 5, 648–655. [PubMed: 23715510]

Huet D, Rajendran E, van Dooren GG, and Lourido S (2018). Identification of cryptic subunits from an apicomplexan ATP synthase. Elife 7.

Huttlin EL, Ting L, Bruckner RJ, Gebreab F, Gygi MP, Szpyt J, Tam S, Zarraga G, Colby G, Baltier K, et al. (2015). The BioPlex Network: A Systematic Exploration of the Human Interactome. Cell 162, 425–440. [PubMed: 26186194]

Hyberts SG, Milbradt AG, Wagner AB, Arthanari H, and Wagner G (2012). Application of iterative soft thresholding for fast reconstruction of NMR data non-uniformly sampled with multidimensional Poisson Gap scheduling. J Biomol NMR 52, 315–327. [PubMed: 22331404]

Hyberts SG, Takeuchi K, and Wagner G (2010). Poisson-gap sampling and forward maximum entropy reconstruction for enhancing the resolution and sensitivity of protein NMR data. J Am Chem Soc 132, 2145–2147. [PubMed: 20121194]

Ingerman E, and Nunnari J (2005). A continuous, regenerative coupled GTPase assay for dynamin-related proteins. Methods Enzymol 404, 611–619. [PubMed: 16413304]

Jao LE, Wente SR, and Chen W (2013). Efficient multiplex biallelic zebrafish genome editing using a CRISPR nuclease system. Proc Natl Acad Sci U S A 110, 13904–13909. [PubMed: 23918387]

Jonckheere V, Fijalkowska D, and Van Damme P (2018). Omics Assisted N-terminal Proteoform and Protein Expression Profiling On Methionine Aminopeptidase 1 (MetAP1) Deletion. Mol Cell Proteomics 17, 694–708. [PubMed: 29317475]

Jordan MR, Wang J, Weiss A, Skaar EP, Capdevila DA, and Giedroc DP (2019). Mechanistic Insights into the Metal-Dependent Activation of Zn(II)-Dependent Metallochaperones. Inorg Chem 58, 13661–13672. [PubMed: 31247880]

Jumper J, Evans R, Pritzel A, Green T, Figurnov M, Ronneberger O, Tunyasuvunakool K, Bates R, Zidek A, Potapenko A, et al. (2021). Highly accurate protein structure prediction with AlphaFold. Nature 596, 583–589. [PubMed: 34265844]

Kabir-ud-Din B,M, Khan IA (2003). Kinetics and mechanism of the ninhydrin reaction with DL-methionine in the absence and the presence of organic solvents. . Indian J Chem 42B, 1132–1136.

Kateb F, Perrin H, Tripsianes K, Zou P, Spadaccini R, Bottomley M, Franzmann TM, Buchner J, Ansieau S, and Sattler M (2013). Structural and functional analysis of the DEAF-1 and BS69 MYND domains. PLoS One 8, e54715. [PubMed: 23372760]

Kim HK, Kim RR, Oh JH, Cho H, Varshavsky A, and Hwang CS (2014). The N-terminal methionine of cellular proteins as a degradation signal. Cell 156, 158–169. [PubMed: 24361105]

Kramer A, Green J, Pollard J Jr., and Tugendreich S (2014). Causal analysis approaches in Ingenuity Pathway Analysis. Bioinformatics 30, 523–530. [PubMed: 24336805]

Krezel A, and Maret W (2017). The Functions of Metamorphic Metallothioneins in Zinc and Copper Metabolism. Int J Mol Sci 18.

Kumar S, Stecher G, Suleski M, and Hedges SB (2017). TimeTree: A Resource for Timelines, Timetrees, and Divergence Times. Mol Biol Evol 34, 1812–1819. [PubMed: 28387841]

Kuzmic P (1996). Program DYNAFIT for the analysis of enzyme kinetic data: application to HIV proteinase. Anal Biochem 237, 260–273. [PubMed: 8660575]

Lee W, Tonelli M, and Markley JL (2015). NMRFAM-SPARKY: enhanced software for biomolecular NMR spectroscopy. Bioinformatics 31, 1325–1327. [PubMed: 25505092]

Leopoldini M, Russo N, and Toscano M (2007). Which one among Zn(II), Co(II), Mn(II), and Fe(II) is the most efficient ion for the methionine aminopeptidase catalyzed reaction? J Am Chem Soc 129, 7776–7784. [PubMed: 17523636]

Li X, and Chang YH (1995). Amino-terminal protein processing in Saccharomyces cerevisiae is an essential function that requires two distinct methionine aminopeptidases. Proc Natl Acad Sci U S A 92, 12357–12361. [PubMed: 8618900]

Lin Z, Gasic I, Chandrasekaran V, Peters N, Shao S, Mitchison TJ, and Hegde RS (2020). TTC5 mediates autoregulation of tubulin via mRNA degradation. Science 367, 100–104. [PubMed: 31727855]

Liu Y, Chen W, Gaudet J, Cheney MD, Roudaia L, Cierpicki T, Klet RC, Hartman K, Laue TM, Speck NA, et al. (2007). Structural basis for recognition of SMRT/N-CoR by the MYND domain and its contribution to AML1/ETO's activity. Cancer Cell 11, 483–497. [PubMed: 17560331]

Livak KJ, and Schmittgen TD (2001). Analysis of relative gene expression data using real-time quantitative PCR and the 2(−Delta Delta C(T)) Method. Methods 25, 402–408. [PubMed: 11846609]

Lo MN, Damon LJ, Wei Tay J, Jia S, and Palmer AE (2020). Single cell analysis reveals multiple requirements for zinc in the mammalian cell cycle. Elife 9.

Lohr F, Hansel R, Rogov VV, and Dotsch V (2007). Improved pulse sequences for sequence specific assignment of aromatic proton resonances in proteins. J Biomol NMR 37, 205–224. [PubMed: 17237975]

Loschen G, Azzi A, Richter C, and Flohe L (1974). Superoxide radicals as precursors of mitochondrial hydrogen peroxide. FEBS Lett 42, 68–72. [PubMed: 4859511]

Maciejewski MW, Schuyler AD, Gryk MR, Moraru II, Romero PR, Ulrich EL, Eghbalnia HR, Livny M, Delaglio F, and Hoch JC (2017). NMRbox: A Resource for Biomolecular NMR Computation. Biophys J 112, 1529–1534. [PubMed: 28445744]

MacLean B, Tomazela DM, Shulman N, Chambers M, Finney GL, Frewen B, Kern R, Tabb DL, Liebler DC, and MacCoss MJ (2010). Skyline: an open source document editor for creating and analyzing targeted proteomics experiments. Bioinformatics 26, 966–968. [PubMed: 20147306]

Meinnel T, and Giglione C (2008). Tools for analyzing and predicting N-terminal protein modifications. Proteomics 8, 626–649. [PubMed: 18203265]

Mirdita M, Ovchinnikov S, and Steinegger M (2021). ColabFold - Making protein folding accessible to all. bioRxiv, 2021.2008.2015.456425

Monteith A, Marszalec W, Chan P, Logan J, Yu W, Schwarz N, Wokosin D, and Hockberger P (2013). Imaging of mitochondrial and non-mitochondrial responses in cultured rat hippocampal neurons exposed to micromolar concentrations of TMRM. PLoS One 8, e58059. [PubMed: 23483968]

Mortensen BL, Rathi S, Chazin WJ, and Skaar EP (2014). Acinetobacter baumannii response to host-mediated zinc limitation requires the transcriptional regulator Zur. J Bacteriol 196, 2616–2626. [PubMed: 24816603]

Muhire BM, Varsani A, and Martin DP (2014). SDT: a virus classification tool based on pairwise sequence alignment and identity calculation. PLoS One 9, e108277. [PubMed: 25259891]

Nyathi Y, and Pool MR (2015). Analysis of the interplay of protein biogenesis factors at the ribosome exit site reveals new role for NAC. J Cell Biol 210, 287–301. [PubMed: 26195668]

O'Halloran TV, and Culotta VC (2000). Metallochaperones, an intracellular shuttle service for metal ions. J Biol Chem 275, 25057–25060. [PubMed: 10816601]

Ogo OA, Tyson J, Cockell SJ, Howard A, Valentine RA, and Ford D (2015). The zinc finger protein ZNF658 regulates the transcription of genes involved in zinc homeostasis and affects ribosome biogenesis through the zinc transcriptional regulatory element. Mol Cell Biol 35, 977–987. [PubMed: 25582195]

Parichy DM, Elizondo MR, Mills MG, Gordon TN, and Engeszer RE (2009). Normal table of postembryonic zebrafish development: staging by externally visible anatomy of the living fish. Dev Dyn 238, 2975–3015. [PubMed: 19891001]

Pelton JG, Torchia DA, Meadow ND, and Roseman S (1993). Tautomeric states of the active-site histidines of phosphorylated and unphosphorylated IIIGlc, a signal-transducing protein from Escherichia coli, using two-dimensional heteronuclear NMR techniques. Protein Sci 2, 543–558. [PubMed: 8518729]

Peroutka Iii RJ, Orcutt SJ, Strickler JE, and Butt TR (2011). SUMO fusion technology for enhanced protein expression and purification in prokaryotes and eukaryotes. Methods Mol Biol 705, 15–30. [PubMed: 21125378]

Picard M, Shirihai OS, Gentil BJ, and Burelle Y (2013). Mitochondrial morphology transitions and functions: implications for retrograde signaling? Am J Physiol Regul Integr Comp Physiol 304, R393–406. [PubMed: 23364527]

Polevoda B, and Sherman F (2003). N-terminal acetyltransferases and sequence requirements for N-terminal acetylation of eukaryotic proteins. J Mol Biol 325, 595–622. [PubMed: 12507466]

Prasad AS (2013). Discovery of human zinc deficiency: its impact on human health and disease. Adv Nutr 4, 176–190. [PubMed: 23493534]

Rachineni K, Arya T, Singarapu KK, Addlagatta A, and Bharatam J (2015). Chemical shift assignments of zinc finger domain of methionine aminopeptidase 1 (MetAP1) from Homo sapiens. Biomol NMR Assign 9, 351–353. [PubMed: 25921012]

Raghunath A, and Perumal E (2018). Analysis of Lethality and Malformations During Zebrafish (Danio rerio) Development. Methods Mol Biol 1797, 337–363. [PubMed: 29896702]

Robert X, and Gouet P (2014). Deciphering key features in protein structures with the new ENDscript server. Nucleic Acids Res 42, W320–324. [PubMed: 24753421]

Rosenzweig AC (2002). Metallochaperones: bind and deliver. Chem Biol 9, 673–677. [PubMed: 12079778]

Sattler M, Schleucher J, Griesinger C (1999). Heteronuclear multidimensional NMR experiments for the structure determination of proteins in solution employing pulsed field gradients. Progress in Nuclear Magnetic Resonance Spectroscopy 34, 93–158.

Scaduto RC Jr., and Grotyohann LW (1999). Measurement of mitochondrial membrane potential using fluorescent rhodamine derivatives. Biophys J 76, 469–477. [PubMed: 9876159]

Schindelin J, Arganda-Carreras I, Frise E, Kaynig V, Longair M, Pietzsch T, Preibisch S, Rueden C, Saalfeld S, Schmid B, et al. (2012). Fiji: an open-source platform for biological-image analysis. Nat Methods 9, 676–682. [PubMed: 22743772]

Sheffield P, Garrard S, and Derewenda Z (1999). Overcoming expression and purification problems of RhoGDI using a family of "parallel" expression vectors. Protein Expr Purif 15, 34–39. [PubMed: 10024467]

Shen Y, and Bax A (2015). Protein structural information derived from NMR chemical shift with the neural network program TALOS-N. Methods Mol Biol 1260, 17–32. [PubMed: 25502373]

Sigel A, Sigel H, and Sigel RKO (2013). Interrelations between essential metal ions and human diseases (Dordrecht ; New York: Springer).

Stetefeld J, McKenna SA, and Patel TR (2016). Dynamic light scattering: a practical guide and applications in biomedical sciences. Biophys Rev 8, 409–427. [PubMed: 28510011]

Sydor AM, Jost M, Ryan KS, Turo KE, Douglas CD, Drennan CL, and Zamble DB (2013). Metal binding properties of *Escherichia coli* YjiA, a member of the metal homeostasis-associated COG0523 family of GTPases. Biochemistry 52, 1788–1801. [PubMed: 24449932]

Towbin H, Bair KW, DeCaprio JA, Eck MJ, Kim S, Kinder FR, Morollo A, Mueller DR, Schindler P, Song HK, et al. (2003). Proteomics-based target identification: bengamides as a new class of methionine aminopeptidase inhibitors. J Biol Chem 278, 52964–52971. [PubMed: 14534293]

Tyanova S, Temu T, Sinitcyn P, Carlson A, Hein MY, Geiger T, Mann M, and Cox J (2016). The Perseus computational platform for comprehensive analysis of (prote)omics data. Nat Methods 13, 731–740. [PubMed: 27348712]

Uhlen M, Fagerberg L, Hallstrom BM, Lindskog C, Oksvold P, Mardinoglu A, Sivertsson A, Kampf C, Sjostedt E, Asplund A, et al. (2015). Proteomics. Tissue-based map of the human proteome. Science 347, 1260419. [PubMed: 25613900]

Ulrich EL, Akutsu H, Doreleijers JF, Harano Y, Ioannidis YE, Lin J, Livny M, Mading S, Maziuk D, Miller Z, et al. (2008). BioMagResBank. Nucleic Acids Res 36, D402–408. [PubMed: 17984079]

UniProt C (2021). UniProt: the universal protein knowledgebase in 2021. Nucleic Acids Res 49, D480–D489. [PubMed: 33237286]

Varshavsky A (2011). The N-end rule pathway and regulation by proteolysis. Protein Sci 20, 1298–1345. [PubMed: 21633985]

Vetro JA, and Chang YH (2002). Yeast methionine aminopeptidase type 1 is ribosome-associated and requires its N-terminal zinc finger domain for normal function in vivo. J Cell Biochem 85, 678–688. [PubMed: 11968008]

Vetro JA, D.B., and Chang Y (2004). Methionine Aminopeptidase Emerging role in angiogenesis. In Aminopeptidases in Biology and Disease, Lendeckel H.a., ed. (New York: Kluwer Academic/Plenum Publishers).

Weissert V, Rieger B, Morris S, Arroum T, Psathaki OE, Zobel T, Perkins G, and Busch KB (2021). Inhibition of the mitochondrial ATPase function by IF1 changes the spatiotemporal organization of ATP synthase. Biochim Biophys Acta Bioenerg 1862, 148322. [PubMed: 33065099]

Wellenreuther G, Cianci M, Tucoulou R, Meyer-Klaucke W, and Haase H (2009). The ligand environment of zinc stored in vesicles. Biochem Biophys Res Commun 380, 198–203. [PubMed: 19171119]

White KN, Tenney K, and Crews P (2017). The Bengamides: A Mini-Review of Natural Sources, Analogues, Biological Properties, Biosynthetic Origins, and Future Prospects. J Nat Prod 80, 740–755. [PubMed: 28185457]

Wong A, Vallender EJ, Heretis K, Ilkin Y, Lahn BT, Martin CL, and Ledbetter DH (2004). Diverse fates of paralogs following segmental duplication of telomeric genes. Genomics 84, 239–247. [PubMed: 15233989]

Xiao Q, Zhang F, Nacev BA, Liu JO, and Pei D (2010). Protein N-terminal processing: substrate specificity of *Escherichia coli* and human methionine aminopeptidases. Biochemistry 49, 5588–5599. [PubMed: 20521764]

Yamazaki T, F.-K.J., Kay LE (1993). Two-dimensional NMR experiments for correlating carbon-13.beta. and proton.delta./.epsilon. chemical shifts of aromatic residues in 13C-labeled proteins via scalar couplings. J Am Chem Soc 115, 11054–11055.

Zhang Y, Griffith EC, Sage J, Jacks T, and Liu JO (2000). Cell cycle inhibition by the anti-angiogenic agent TNP-470 is mediated by p53 and p21WAF1/CIP1. Proc Natl Acad Sci U S A 97, 6427–6432. [PubMed: 10841547]

Zougman A, Selby PJ, and Banks RE (2014). Suspension trapping (STrap) sample preparation method for bottom-up proteomics analysis. Proteomics 14, 1006–1000. [PubMed: 24678027]

Highlights

- The N-terminus of ZNG1 interacts with the zinc finger of METAP1
- ZNG1 activates METAP1 activity in a Zn- and GTP-hydrolysis dependent manner
- Loss of ZNG1 impairs mitochondrial function and cellular proliferation
- *Zng1* mutant animals are sensitive to Zn starvation and inhibition of METAP activity

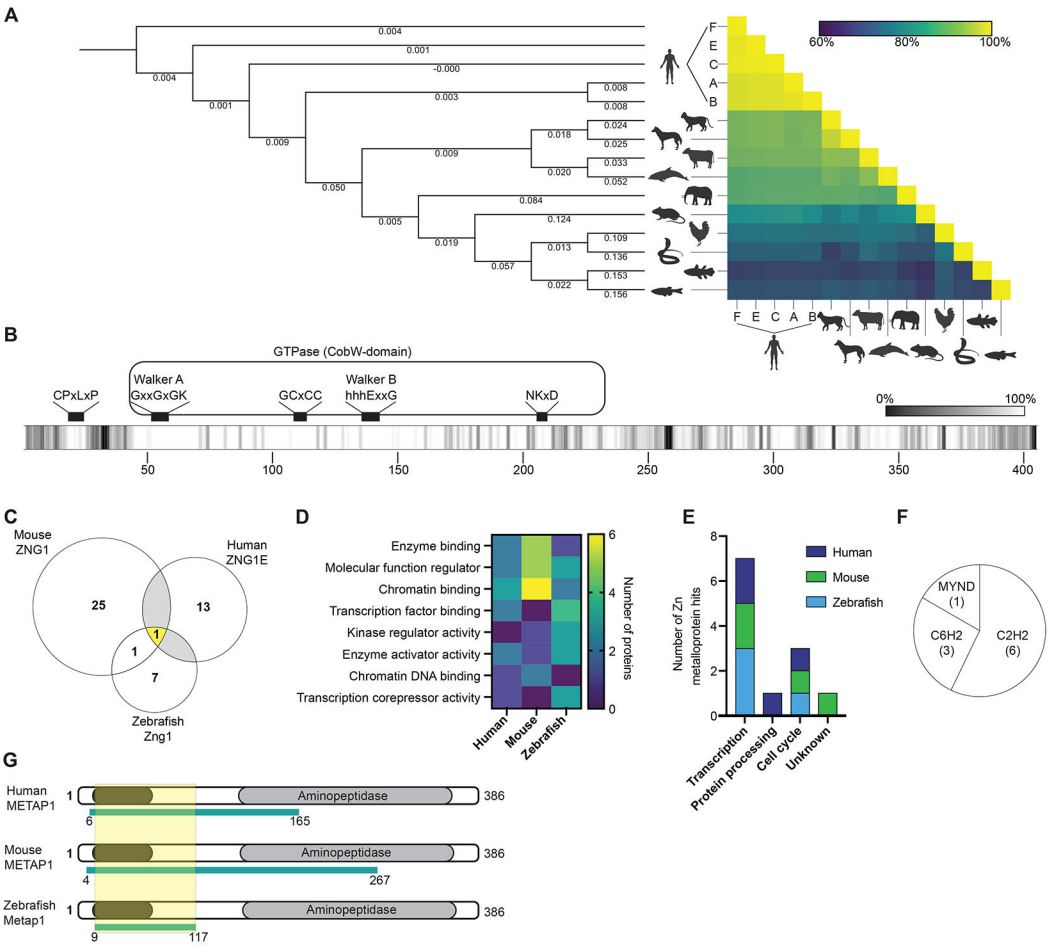

Figure 1. Identification of metalloprotein targets of Zn regulated GTPase metalloprotein activator 1 (ZNG1) in vertebrates.

(A) Cladogram and analysis of ZNG1 protein sequence conservation in vertebrates. Numbers on branches denote nucleotide substitutions per site. **(B)** Amino acid conservation along the length of vertebrate ZNG1s indicates high sequence conservation particularly in the GTPase domains and at the N-terminus. Lighter shading reflects higher conservation. **(C)** Yeast-two-hybrid screens using full-length human, mouse, and zebrafish ZNG1s identify unique and shared interacting proteins. **(D)** Molecular function enrichment analysis of ZNG1 interaction protein PFAM domains. **(E)** Number and cellular activity of ZNG1 client Zn metalloproteins detected in yeast-two-hybrid screens. **(F)** ZNG1 zf interaction domains in Zn metalloproteins shown in E. **(G)** Conserved ZNG1 interaction domain of METAP1 across species overlaps with a C6H2 domain. Yellow shading indicates minimal conserved region. See also Figure S1 and Table S1.

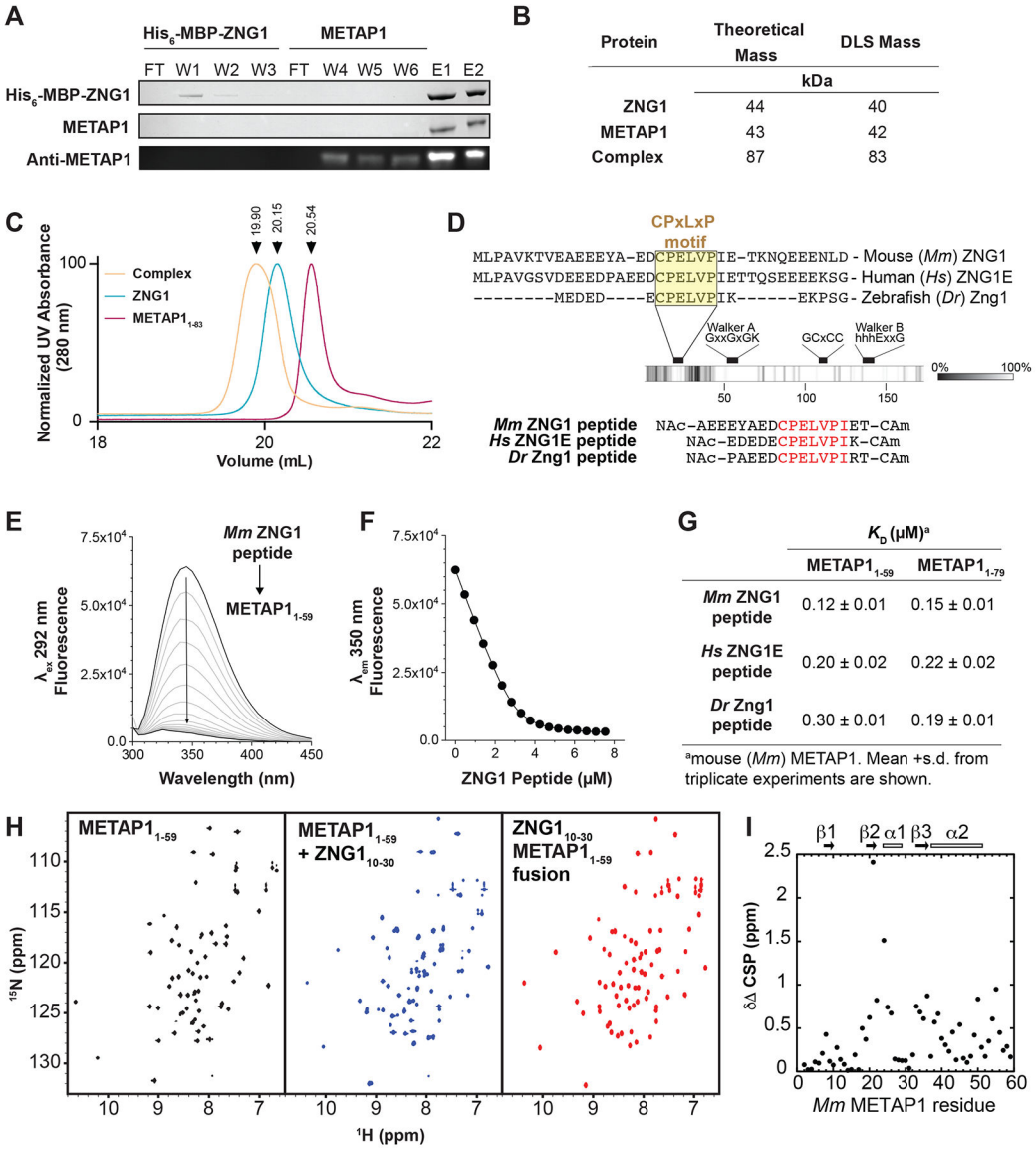

Figure 2. ZNG1 interacts with METAP1 via a unique C6H2 Zn finger domain.

(A) Affinity chromatography of mouse *(Mm)* His-MBP-ZNG1 bound to amylose resin with purified *Mm* METAP1. Detection by SDS PAGE (top 2 panels) and immunoblot (bottom). W-wash, F-flow through, E-elution. **(B)** DLS analysis of full-length *Mm* ZNG1 and METAP1 shows complex formation *in vitro*. **(C)** Size exclusion chromatography of full-length *Mm* ZNG1 and METAP1$_{1\text{-}83}$. **(D)** Identification of a conserved N-terminal 'CPELVPI' motif in *Mm*, human (*Hs*), and zebrafish (*Dr*) ZNG1s and synthetic peptides. **(E)** Spectra of W45 fluorescence quenching of 3 μM METAP1$_{1\text{-}59}$ upon *Mm* ZNG1 N-terminus binding. **(F)** Peptide binding curve from (E) fit to a 1:1 binding model. **(G)** Measured affinities of METAP1$_{1\text{-}59}$ and METAP1$_{1\text{-}79}$ binding to *Mm, Hs*, and *Dr* ZNG1 N-termini. **(H)** ^{1}H ^{15}N HSQC NMR spectra of METAP1$_{1\text{-}59}$ alone (left), in complex with *Mm* ZNG1 N-terminal peptide (middle), and as N-terminal *Mm* ZNG1 peptide fusion

(right). **(I)** Chemical shift perturbations in ^{15}N METAP1$_{1\text{-}59}$ upon binding to *Mm* ZNG1 peptide. See also Figure S2.

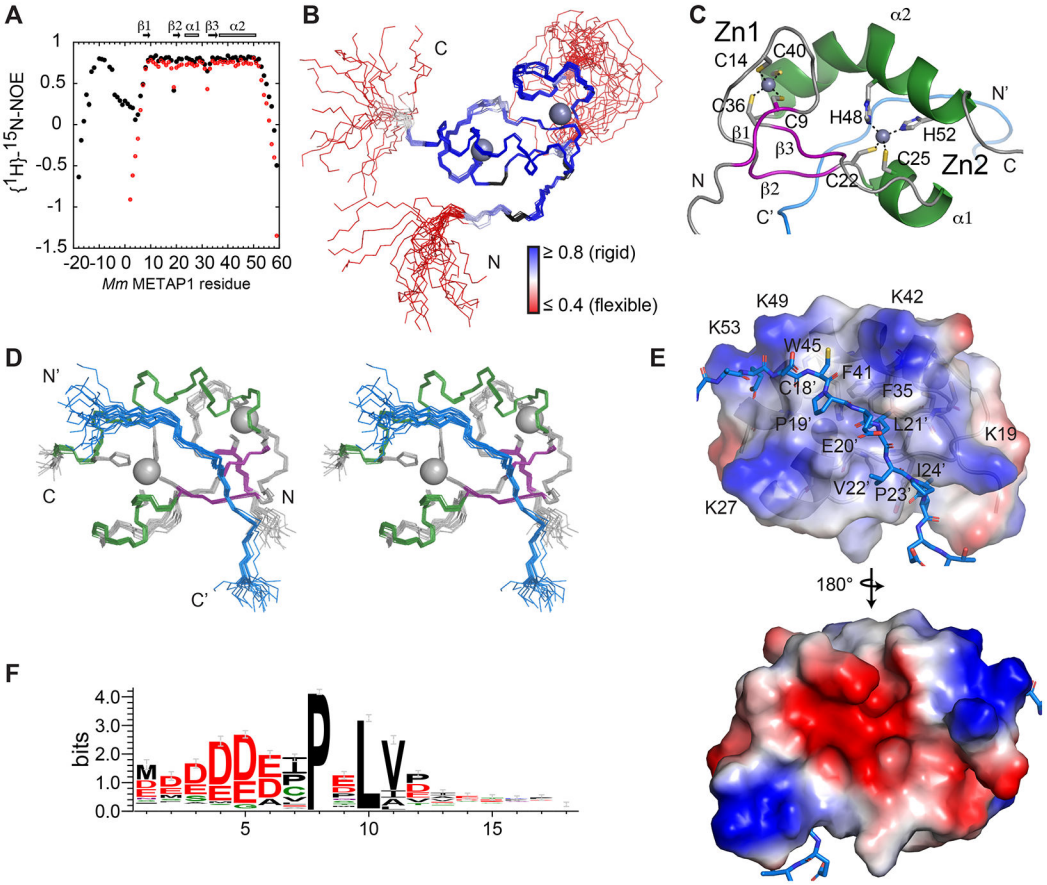

Figure 3. NMR structure of METAP1-ZNG1 complex.

(A) ^{1}H,^{15}N NOE for the fusion (black) and free domain (red). **(B)** Structure of the 20 lowest-energy conformers of the *Mm* ZNG1$_{10-30}$ METAP1$_{1-59}$ fusion, colored by ^{1}H,^{15}N NOE. **(C)** Ribbon diagram of *Mm* ZNG1$_{10-30}$ METAP1$_{1-59}$ showing Zn coordination. **(D)** Stereo view of 20 lowest-energy conformers of *Mm* ZNG1$_{10-30}$ METAP1$_{1-59}$, colored by secondary structure, with helices in green, beta strands in purple, and peptide in blue. **(E)** Electrostatic surface map of the METAP1$_{1-59}$ peptide interface. **(F)** N-terminal ZNG1 motif among eukaryotic cluster 3 COG0523 proteins. See also Figure S3 and Table S2.

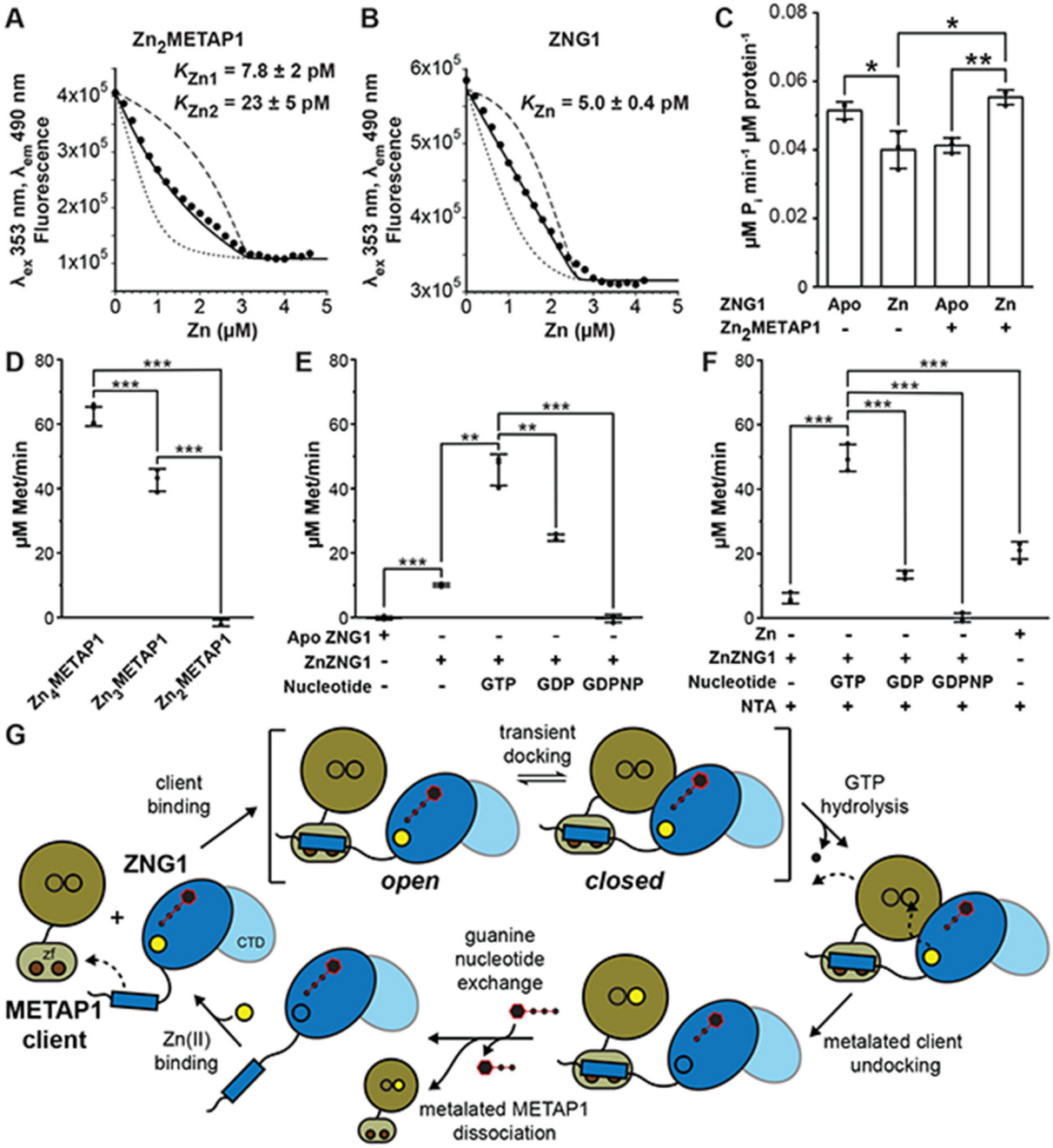

Figure 4. ZNG1 enhances METAP1 aminopeptidase activity *in vitro*.

(A) Representative titration of 1.0 μM METAP1, 1.0 μM quin-2 with Zn. **(B)** Representative titration of 1.3 μM ZNG1, 1.3 μM quin-2 with Zn. Solid lines are global fits of independent replicates; dashed lines are simulations of 10-fold greater and weaker affinities. **(C)** GTPase activity of ZNG1 with or without Zn and/or Zn_2METAP1. **(D)** Initial rate of Met release from 750 μM MAHAIHY peptide by 20 nM METAP1 in different metalation states. **(E)** Activation of 10 μM Zn_2METAP1 by 25 μM ZNG1 with or without Zn and 500 μM guanine nucleotides. **(F)** Activation of 10 μM Zn_2METAP1 by 22.5 μM Zn or 25 μM ZnZNG1 with or without 500 μM guanine nucleotides, all with 250 μM NTA. In panels E and F,

activation reactions were diluted to 20 nM METAP1 prior to monitoring cleavage of 750 μM MAHAIHY. **(G)** Mechanistic model of GTP hydrolysis-coupled Zn transfer from ZNG1 to the METAP1 active site. See also Figure S4.

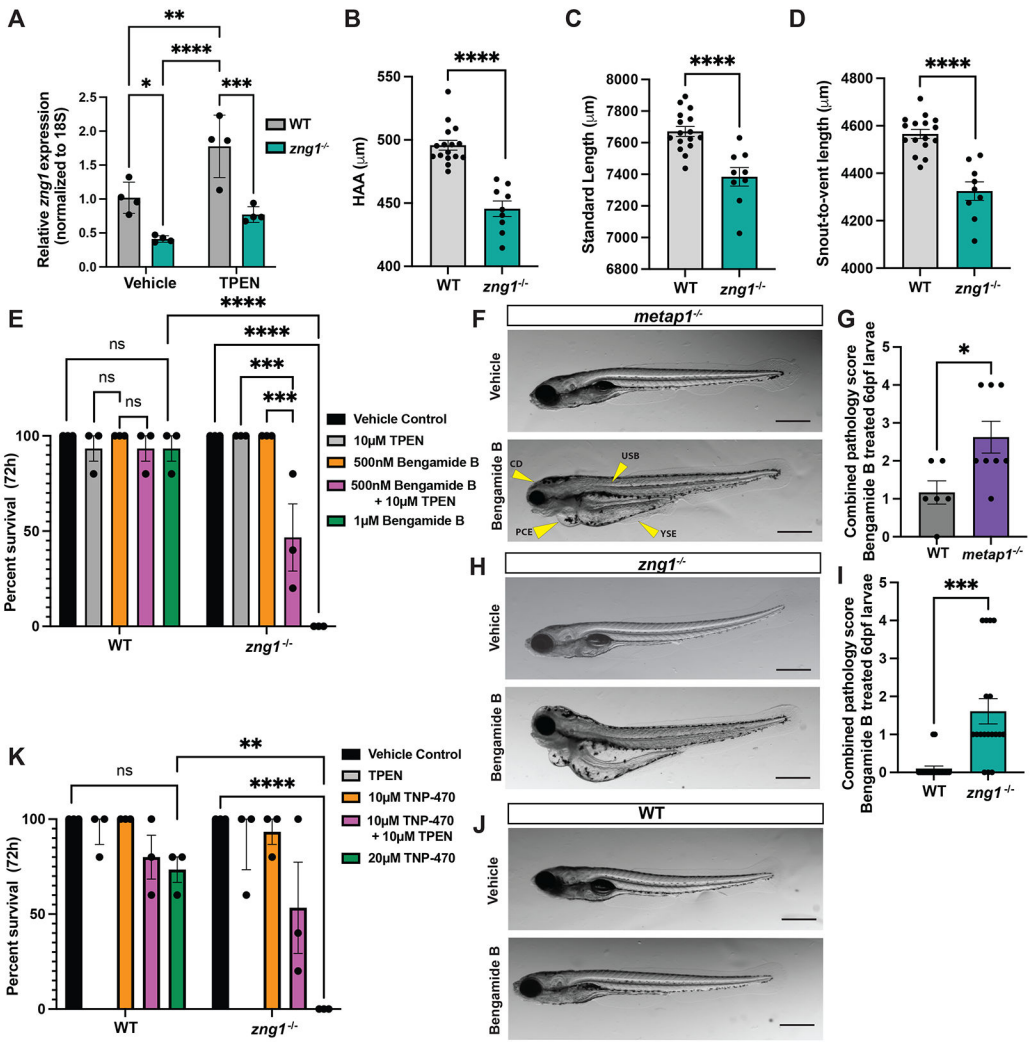

Figure 5. *zng1* mutant zebrafish display Zn-dependent sensitivity to Metap inhibition and phenocopy *metap1* mutant larvae.

(A) *zng1* expression levels measured by RT-qPCR in TPEN treated WT and *zng1*$^{-/-}$ mutant 6 dpf whole zebrafish larvae. (n=4 pools of 30 larvae per genotype / treatment group). **(B-D)** Height at anterior anal fin (HAA) (B), standard length (C), and snout to vent length (D) of *zng1*$^{-/-}$ and WT 6 dpf larvae. Each data point represents an individual larva. **(E)** Survival of WT and *zng1*$^{-/-}$ mutant larvae treated with Bengamide B and TPEN (n=3 groups of 5 larvae / genotype / treatment) over 3 days of treatment and terminating at 6 dpf. **(F)** Brightfield images of 6 dpf *metap1* mutant larvae treated with 1 μM Bengamide B or vehicle control. Yellow arrows denote abnormal pathologies. Pericardial Edema (PCE), craniofacial defects (CD), yolk sack edema (YSE), and uninflated swim bladder (USB). Scale bars = 1 mm. **(G)** Quantification of gross pathology score of 6 dpf Bengamide B treated *metap1* mutant and WT larvae. Pathology scores calculated as sum of each pathology indicated by the yellow arrows in panel F. Each data point represents an individual larva. **(H)** Brightfield images of 6 dpf *zng1* mutant larvae treated with 500 nM Bengamide B or vehicle control. Scale bars = 1 mm. **(I)** Quantification of gross pathology score of 6 dpf Bengamide B

treated *zng1* mutant larvae as depicted above. **(J)** Brightfield images of 6 dpf WT larvae treated with 1 μM Bengamide B or vehicle control. Scale bars = 1mm. **(K)** Survival of WT and *zng1*$^{-/-}$ larvae treated with TNP-470 and TPEN (n=3 groups of 5 larvae / genotype / treatment) over 3 days of treatment and terminating at 6 dpf. Data in panels A, E, and K analyzed by two-way ANOVA with Tukey's multiple comparison test. Data in panels B,C,D, G and I analyzed by Student's *t*-test. See also Figure S5.

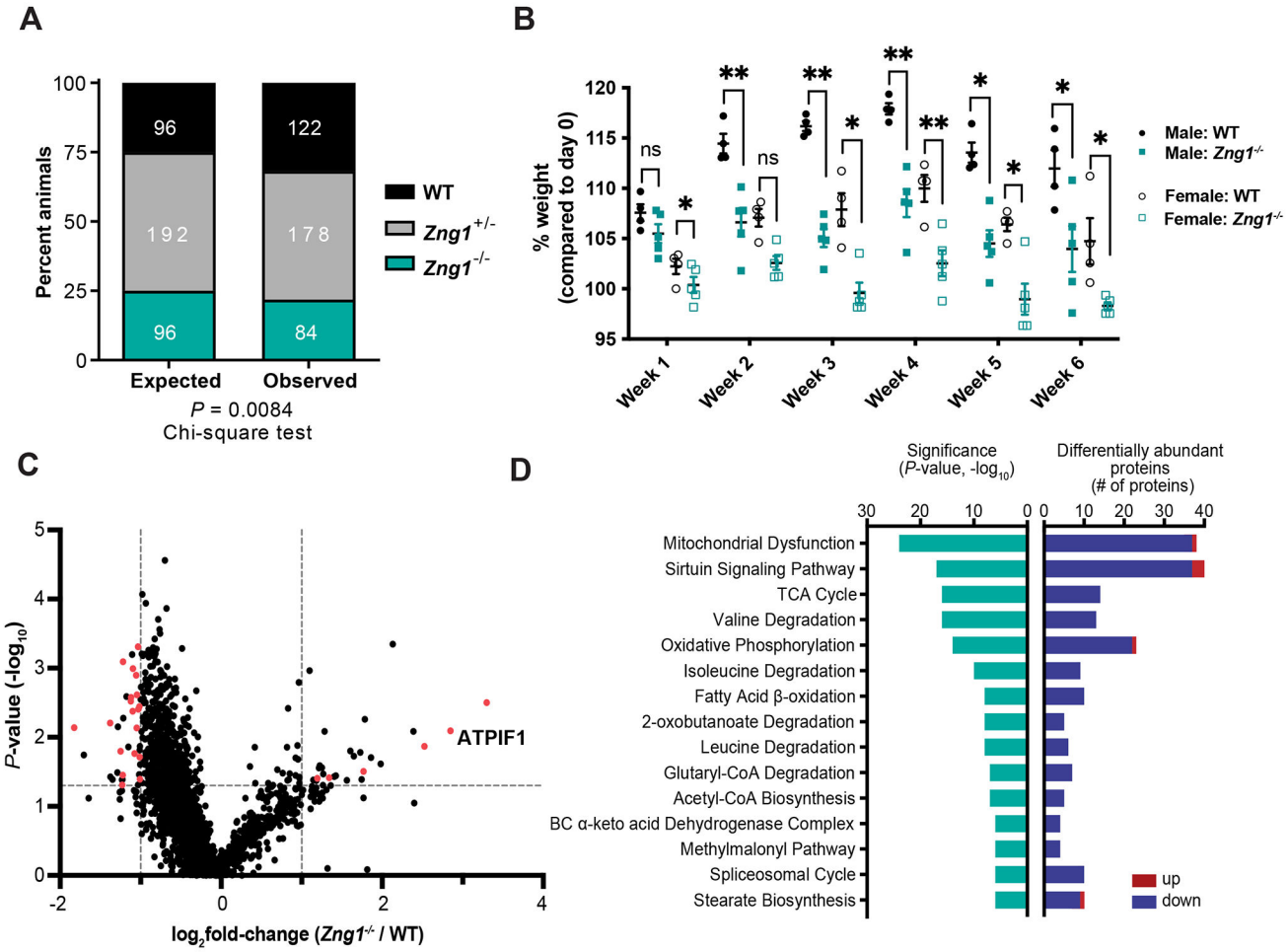

Figure 6. *Zng1* mutant mice exhibit signatures of mitochondrial dysfunction on a Zn deficient diet.

(A) Genotype distribution of WT, *Zng1*$^{+/-}$, and *Zng1*$^{-/-}$ mice. Number of animals per genotype indicated in white text. **(B)** Percent weight gain of 5-7 week old WT and *Zng1* mutant mice that were placed on a Zn-deficient diet for 6 weeks (n= 4-5 mice / genotype / sex). **(C)** Differential protein abundances from dissected kidneys of 11-13 week old female WT and *Zng1* mutant mice that were maintained on a low Zn diet for 5 weeks. Proteins that putatively localize to the mitochondria are highlighted in red (n = 5 mice / genotype). **(D)** IPA analysis of differentially abundant proteins (*Zng1*$^{-/-}$/WT) with significance of gene enrichment and number of differentially abundant proteins for each pathway depicted. z-scores are denoted within teal bars and indicate the predicted effects on each pathway (positive values: activation; negative values: inhibition, n.a.: no prediction through IPA available due to insufficient evidence in the Knowledge Base). Red bars indicate enriched proteins in *Zng1* mutant animals and blue bars represent proteins with reduced abundance. Data in panel A analyzed by Chi-squared goodness of fit test. Data in panel B analyzed by two-way ANOVA with Sidak's multiple comparison test within each sex. See also Figure S6 and Table S3.

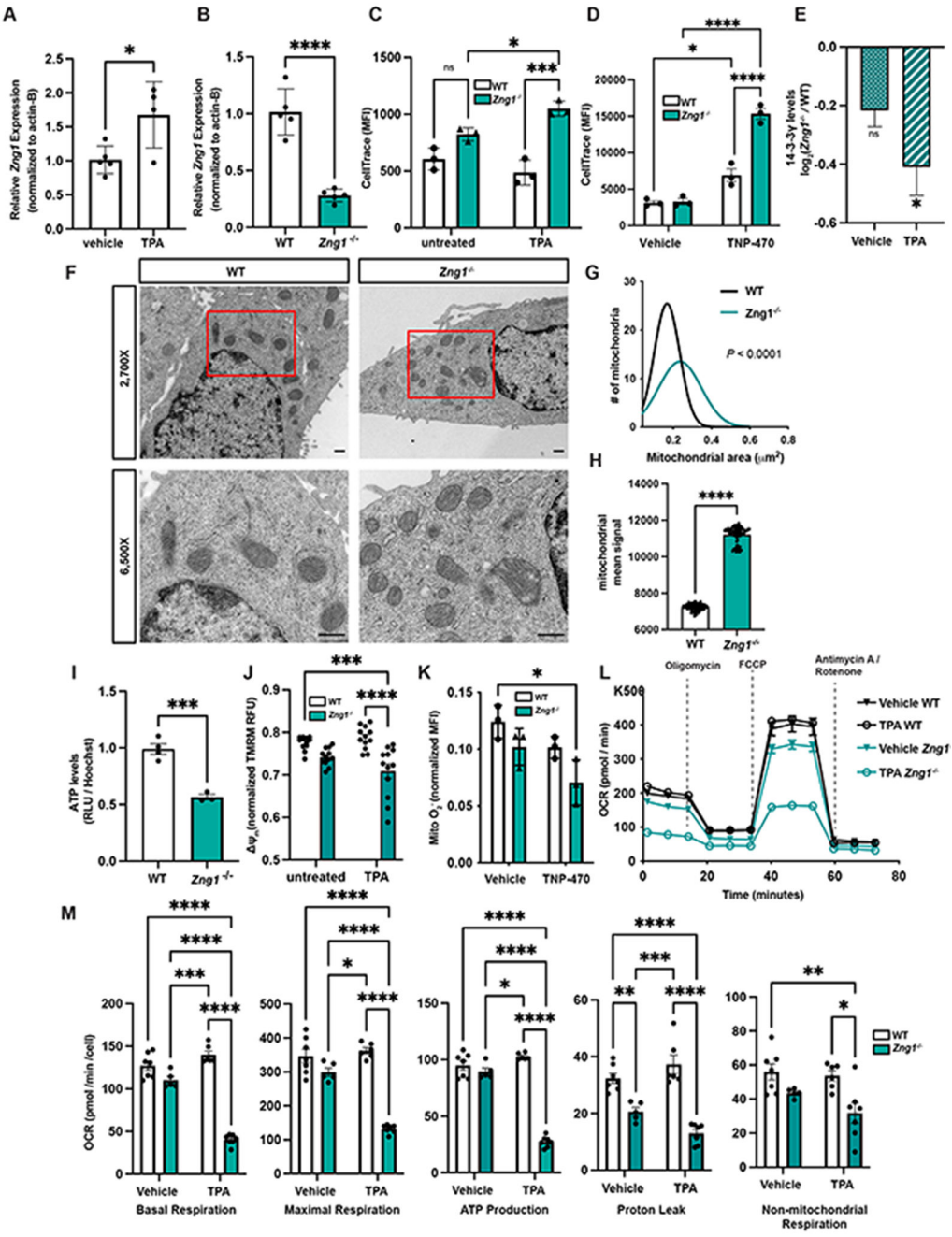

Figure 7. ZNG1 regulates cellular respiration through stimulation of METAP activity.

(A) Expression of *Zng1* in TKPTS cells treated with TPA. **(B)** *Zng1* transcript levels in untreated WT and *Zng1* mutant cells. **(C-D)** Cell proliferation quantified by CellTrace median fluorescence intensity (MFI) in Zn-deplete conditions (C) and following treatment with METAP2 inhibitor TNP-470 (D) using flow cytometry. **(E)** Ratio of processed 14-3-3γ protein levels in vehicle or TPA treated $Zng1^{-/-}$ /WT cells. (n = 4 / genotype / treatment). **(F)** Representative TEM images of WT and *Zng1* mutant cells grown in Zn-deplete conditions (scale bars = 500 nm). Red box (top panel) outlines region of higher magnification (bottom panel). **(G-H)** Non-linear regression analysis of the size distribution

of mitochondria (G) and mean signal intensity (H) in WT and *Zng1* mutant cells treated with TPA. (WT n = 112 mitochondria, $Zng1^{-/-}$ n = 101 mitochondria). **(I)** ATP levels in cell lysates from untreated WT and *Zng1* mutant cells. **(J)** Mitochondrial membrane potential ($\Delta\Psi_m$) in untreated and TPA treated cells. **(K)** Production of mitochondrial superoxide in cells treated with TNP-470 was quantified by flow cytometry. **(L-M)** Oxygen consumption rates (OCR) by cells treated with vehicle or TPA. OCR was normalized by cell number. Data in panels A, B, H, and I analyzed by Student's *t*-test. Data in panel E analyzed by Welch's *t*-test. Data in panel G analyzed by non-linear regression goodness of fit. Data in panels C, D, J, K, and M analyzed by two-way ANOVA with Tukey's multiple comparison test. See also Figure S7 and Table S3.

Key resources table

REAGENT or RESOURCE	SOURCE	IDENTIFIER
Antibodies		
anti-CBWD1	Sigma	CAT#HPA042813, RRID:AB_2678181
anti-OxPhos Complex V inhibitor mouse IgG1 clone 5E2	Invitrogen	CAT# A21355, RRID:AB_1501857
Polyclonal METAP1 antibody	Invitrogen	CAT#PAS-58202
Goat anti-Mouse IgG alexa 555	Invitrogen	CAT# A21424
IRDye 800CW Donkey anti-Rabbit	Li-Cor	CAT#926-32213, RRID:AB_621848
IRDye 680LT Goat anti-Mouse	Li-Cor	CAT#926-68020
anti-Tubulin	Cell signaling	CAT#3873S
Bacterial and virus strains		
E. coli DH5a	Gift from Dr. Olaf Schneewind	N/A
E. coli BL21	Gift from Dr. Olaf Schneewind	N/A
Chemicals, peptides, and recombinant proteins		
Fmoc-Amino acids	Vivitide	CAT# CT01-001 CT04-001 CT03-001 CT4-001 CT07-001 CT11-001 CT10-001 CT17-001 CT15-001 CT20-001 CT19-001
N,N'-Diisopropylcarbodiimide (DIC)	Chem-Impex International	CAT#00110
Ethyl (hydroxyimino)cyanoacetate Oxyma	Aapptec	CAT#CXZ021
Trifluoroacetic acid	Chem-Impex International	CAT#00289
n-Methyl, 2-Pyrrolidone (NMP)	Pharmco	CAT#253000ACS
Acetonitrile	Fisher Chemical	CAT#UN1648
Methylene Chloride (DCM)	Fisher Chemical	CAT#UN1593
Cell Trace Violet	Invitrogen	CAT#C34557
MitoSOX	Thermofisher	CAT#M36008
MitoTracker™ Deep Red FM	Invitrogen	CAT#M22426
TNP-470	Sigma	CAT#T1455-5MG
Bengamide B	Santa cruz	CAT#sc-397521A
N,N,N′,N′-Tetrakis(2-pyridylmethyl)ethylenediamine (TPEN)	Sigma	CAT#P4413
Tris(2-pyridylmethyl)amine	Sigma	CAT#723134
Tetramethylrhodamine methyl ester (TMRM)	Invitrogen	CAT#T668
DpnII	New England Biolabs	CAT#R0543S
Trifluoroacetic acid	Sigma	CAT#299537
IPTG	Roche	CAT#11411446001
Acetonitrile	Fisher	CAT#A998-4

REAGENT or RESOURCE	SOURCE	IDENTIFIER
Tri Reagent	Sigma	CAT#T9424
Amylose resin	New England Biolabs	CAT#E8021L
OPTIMA Nitric Acid	Fisher	CAT#A467-500
Ultratrace Hydrogen Peroxide	Sigma	CAT#95321
UltraPure Water	Invitrogen	CAT#10977-023
ARISTAR ICP Standard Mix	VWR	CAT#BDH82026-108
Sodium Cacodylate Trihydrate	Electron Microscopy Sciences	CAT#12310
Glutaraldehyde	Electron Microscopy Sciences	CAT#16310
Tannic Acid	Electron Microscopy Sciences	CAT#21700
Osmium Tetroxide	Electron Microscopy Sciences	CAT#19110
Uranyl Acetate	Electron Microscopy Sciences	CAT#22400
Propylene Oxide	Electron Microscopy Sciences	CAT#20411
Quetol 651	Electron Microscopy Sciences	CAT#20440
ERL4221	Electron Microscopy Sciences	CAT#15004
Nonenyl Succinic Anhydride	Electron Microscopy Sciences	CAT#19050
DER 736	Electron Microscopy Sciences	CAT#13000
Benzyldimethylamine	Electron Microscopy Sciences	CAT#11400
Lead Nitrate	Electron Microscopy Sciences	CAT#17900
Sodium Citrate	Electron Microscopy Sciences	CAT#21140
Ethanol	Decon Labs	CAT#2716
GTP	Sigma	CAT#10106399001
NADH	Sigma	CAT#N8129
phosphoenolpyruvate	Sigma	CAT#86007
Pyruvate kinase / lactate dehydrogenase	Sigma	CAT#P0294
TCEP	Chem-Impex	CAT#23004
Quin-2	Sigma	CAT#08520
Mag-fura-2	Invitrogen	CAT#M1290
EDTA	Alfa Aesar	CAT#A173850B
Chelex	Bio-Rad	CAT#141253
ZnCl2	Sigma	CAT#208086-100G
Magnesium chloride	Fisher	CAT#AA1079714
Ninhydrin	Sigma	CAT#151173-10G
Malachite green oxalate	Fisher	CAT#229780250
Ammonium molybdate	Sigma	CAT#277908-5G
Phosphate	Fluka	CAT#HONCE3039-100ML
Geneticin sulfate G418	Fisher	CAT#10131035
Lipofectamine 3000	Invitrogen	CAT#L3000-008
Insulin	Sigma	CAT#SLCF5002
Fetal Bovine Serum (FBS)	R and D Systems	CAT#S11150

REAGENT or RESOURCE	SOURCE	IDENTIFIER
Hepes	Fisher	CAT#BP310-500
Lysozyme	ThermoFisher	CAT#89833
HisPur Cobalt Resin	ThermoFisher	CAT#89964
Maltose	Sigma	CAT#63423-100mL
HRV 3C Protease	Pierce	CAT#88947
Nitrilotriacetic acid (NTA)	Sigma	CAT#9877
RIPA	ThermoFisher	CAT#89900
Halt Protease Inhibitor	ThermoFisher	CAT#78442
Tris/Glycine/SDS Buffer	Bio-Rad	CAT#1610732
Ponceau S Solution	Sigma	CAT#P7170
Odyssey Blocking Buffer	Li-Cor	CAT#927-40000
Glacial Acetic acid	Millipore	CAT#AX0074-2
Citric Acid	Sigma	CAT#Z1909
DMSO	Fisher	CAT#D136
Phenol:chloroform:IAA	Fisher	CAT#BP17521-100
4% Paraformaldehyde	Alfa Aesar	CAT#J61899
2X iQ SYBR Green SuperMix	Bio-Rad	CAT#170882
Critical commercial assays		
Seahorse XF Cell Mito Stress Test Kit	Agilent	CAT#103015-100
Pierce™ HRV 3C Protease Solution Kit (2 units/μL)	ThermoFisher	CAT#88946
Deposited data		
NMR chemical shifts (free zinc finger) & backbone relaxation rates	BioMagResBank	51117
NMR chemical shifts (bound zinc finger)	BioMagResBank	51118
NMR chemical shifts (fusion)	BioMagResBank	30956
NMR backbone relaxation rates (fusion)	BioMagResBank	51119
ZNG1-METAP1-zf fusion structure	Protein Data Bank	7SEK
Murine kidney and TKPTS cell line proteomics	ProteomeXchange	562287
Experimental models: Cell lines		
Mouse: TKPTS WT parent	ATCC	CRL-3361
Mouse: TKPTS *Zng1* (−2/−2)	This manuscript	N/A
Mouse: TKPTS *Zng1* (−7/−2)	This manuscript	N/A
Mouse: TKPTS *Zng1* (−2/−2) ; *cmv.Zng1*	This manuscript	N/A
Experimental models: Organisms/strains		
Zebrafish: *zng1* (−5)	This manuscript	N/A
Zebrafish: *metap1* (−17)	This manuscript	N/A
Zebrafish: *zng1*(−11)	This manuscript	N/A
Mouse: *Zng1* (−180)	This manuscript	N/A
Oligonucleotides		
See Table S5 for oligonucleotides	N/A	N/A

REAGENT or RESOURCE	SOURCE	IDENTIFIER
Recombinant DNA		
Mouse: pcDNA3.1-C-(k)-DYK-Cbwd1	GenScript	OMu12215
Mouse: pcDNA3.1-C-(k)-DYK-Metap1	GenScript	OMu05035
Zebrafish: pCRII - *zng1*	This manuscript	N/A
pLM302 zebrafish *zng1*	This manuscript	N/A
pLM302 zebrafish *metap1*	This manuscript	N/A
pLM302 mouse *Zng1*	This manuscript	N/A
pLM302 mouse *Metap1*	This manuscript	N/A
pBG102 mouse *Metap1* 1-83	This manuscript	N/A
pSUMO mouse *Metap1*	This manuscript	N/A
pSUMO mouse *Metap1* 1-59	This manuscript	N/A
pSUMO mouse *Metap1* 1-79	This manuscript	N/A
pSUMO mouse *Zng1* 10-30 *Metap1* 1-59 fusion	This manuscript	N/A
Tagless pHis mouse Zng1 (NdeI-BamHI)	This manuscript	N/A
pT3TS-nls-zCas9-nls	Addgene	CAT#46757
Software and algorithms		
Dynamics 7.5	Wyatt Technologies	DYNAMICS Software - Wyatt Technology
Fiji	Open Source (ImageJ)	Fiji (imagej.net)
ChromLab Software	Bio-Rad	ChromLab Software | Bio-Rad Laboratories
NMRBox	University of Connecticut Health Center	https://nmrbox.org/
HMMER	HMMER	http://hmmer.org/
Topspin 4	Bruker	https://www.bruker.com/en/products-and-solutions/mr/nmr-software/topspin.html
hmsIST	Harvard Medical School	https://bionmr.cores.ucla.edu/?page_id=440
NMRPipe	National Institute of Standards and Technology	https://www.ibbr.umd.edu/nmrpipe/index.html
CARA	https://wuthrich-group.ethz.ch/	http://cara.nmr.ch/
NMRFAM-Sparky	University of Wisconsin	https://nmrfam.wisc.edu/nmrfam-sparky-distribution/
CYANA	LA Systems	http://www.cyana.org
NUS Poisson Gap Sampling Schedule generator for Topspin	Hyberts et al., 2010	https://github.com/nomadiq/nusPGS_TS3_TS4_Distro
IMOD	University of Colorado	https://bio3d.colorado.edu/imod/
SerialEM	University of Colorado	https://bio3d.colorado.edu/SerialEM/
Wave Desktop Software	Agilent Technologies	https://www.agilent.com/en/product/cell-analysis/real-time-cell-metabolic-analysis/xf-software/seahorse-wave-desktop-software-740897

REAGENT or RESOURCE	SOURCE	IDENTIFIER
CLC Genomics Workbench	Qiagen	https://digitalinsights.qiagen.com/products-overview/discovery-insights-portfolio/analysis-and-visualization/qiagen-clc-genomics-workbench/
Ingenuity Pathway Analysis (IPA)	Qiagen	https://digitalinsights.qiagen.com/products-overview/discovery-insights-portfolio/analysis-and-visualization/qiagen-ipa/
Agilent Mass Hunter Workstation Software version A.01.02	Agilent	https://www.agilent.com/en/product/atomic-spectroscopy/inductively-coupled-plasma-mass-spectrometry-icp-ms/icp-ms-software/icp-ms-masshunter-software
BioRender	BioRender	BioRender.com
Other		
HisTrap™ High Performance	Cytiva: Research & Biopharmaceutical Manufacturing	HisTrap HP His tag protein purification columns | Cytiva (cytivalifesciences.com)
HisPur™ Cobalt Resin	Cytiva: Research & Biopharmaceutical Manufacturing	HisPur™ Cobalt Resin (thermofisher.com)
Superdex 200 Increase 10/300 GL	Cytiva: Research & Biopharmaceutical Manufacturing	Superdex 200 Increase 10/300 GL | Cytiva (cytivalifesciences.com)
NGC Quest 10	Bio-Rad	NGC Quest 10 Chromatography System | Bio-Rad Laboratories
DynaPro NanoStar	Wyatt Technologies	DynaPro NanoStar Dynamic Light Scattering Detector for Nanoparticles (wyatt.com)
Supelco Ascentis Express C18 Column (50 mm x 2.1 mm, 5 micro particles)	Sigma	50509-U
SecurityGuard C18 Cartridge (3.2 mm x 8 mm)	Phenomenex	AJ0-4287